Scientific Reports

https://doi.org/10.1038/s41598-026-56136-x

Article in Press

Multi-wavelength architecture of the tensional stress field of peninsular Italy

Received: 23 March 2026

Accepted: 29 May 2026

Published online: 09 June 2026

Cite this article as: Lavecchia G., Andrenacci C., Bello S. *et al.* Multi-wavelength architecture of the tensional stress field of peninsular Italy. *Sci Rep* (2026). https://doi.org/10.1038/s41598-026-56136-x

Giusy Lavecchia, Carlo Andrenacci, Simone Bello, Federico Pietrolungo, Francesco Brozzetti & Rita Nardis

Multi-Wavelength Architecture of the Tensional Stress Field of Peninsular Italy

Giusy Lavecchia[1†], Carlo Andrenacci[1,2†], Simone Bello[1,2,3]*, Federico Pietrolungo[1,4], Francesco Brozzetti[1,2], Rita de Nardis[1,2]

[1]Centro inteRUniversitario per l'analisi Sismotettonica Tridimensionale (CRUST), Chieti, Italy

[2]Dipartimento di Scienze, University G. d'Annunzio Chieti – Pescara, 66100, Chieti, Italy

[3]Istituto di Geologia Ambientale e Geoingegneria (IGAG), Consiglio Nazionale delle Ricerche (CNR), Monterotondo, Rome, Italy

[4]Istituto Nazionale di Geofisica e Vulcanologia, INGV, Rome, Italy

[†]Co-first Author

*Corresponding author: simone.bello@unich.it

Abstract

Understanding how stress is organized and maintained within the continental lithosphere remains a central challenge in geodynamics, seismotectonics and seismic hazard assessment, yet regional models rarely resolve full stress tensors or capture their long-term persistence. Using a uniquely dense dataset of ~8,200 geological fault-slip measurements integrated within a hierarchical, multi-scale fault architecture framework, we define the boundary of the ~1000 km-long Intra-Apennine Extensional Province (IEP) of Italy and reconstruct the spatial pattern of principal stress orientations and relative magnitudes over the last ~3.5 Ma. Stress tensors resolved from outcrop to regional scale reveal a persistent Andersonian tensional regime and a nested, multi-wavelength arcuate organization of the stress field. Fault-scale rotations, segment-scale curvature, and a crustal-scale double arc broadly parallel to Moho geometry indicate strong coupling between deep structural architecture and upper-crustal deformation. An earlier transtensional stage is distinguished from the long-lived dip-slip tensional phase that shapes the present seismogenic framework. Comparison with earthquake focal mechanisms and GNSS-derived strain rates reveals strong directional coherence between geological stress indicators over time and ongoing deformation. These findings establish geological stress inversion as a powerful tool for imaging active lithospheric stress architectures and provide a transferable framework for interpreting intraplate extension and related seismogenic fault systems worldwide.

Keywords

Geological stress inversion; Multi-scale fault architecture; Faults and fault-slip data; Intraplate extension; Stress-strain T-axis hybrid map; Apennines, Italy

Running Title

Multi-scale Stress Architecture in the Intra-Apennine Extensional Province

Summary sentence

By integrating multi-scale geological stress inversion with fault-system architecture, we reveal a long-lived, crust-scale Andersonian tensional stress field coherently linking fault systems, seismicity, and present-day deformation across the Italian Apennines, providing new constraints on intraplate extension and seismogenic faulting.

INTRODUCTION

Understanding whether active stress fields persist, reorganize, or decay over geological timescales remains a fundamental and unresolved question in geodynamics and seismotectonics. While regional stress compilations have substantially advanced our knowledge of present-day intraplate deformation[1,2], they are largely derived from focal mechanisms and geodetic data[3,4,5,6]. These datasets sample short temporal windows and commonly resolve only horizontal stress orientations, thereby limiting constraints on full stress tensors and their long-term continuity within an actively deforming lithosphere[7]. As a consequence, the mechanical relationships between time-integrated geological deformation and present-day stress are still debated.

Geological fault-slip data may provide a complementary, time-integrated record of brittle deformation. When systematically organized across spatial scales and explicitly linked to fault architecture, they have the potential to discriminate between transient stress perturbations and persistent regional stress regimes. However, geological stress indicators are often regarded as paleostress proxies and are rarely incorporated into regional seismotectonic stress models. Whether such data can resolve active stress architectures over millions of years, rather than merely reconstruct fossil deformation phases, remains an open problem. The Late Pliocene–Quaternary Intra-Apennine Extensional Province (IEP) of Italy offers a natural laboratory to address this issue[8,9] (Fig.1). This ~1000 km-long intraplate extensional belt, affected by recurrent Mw 6.0-7.0 earthquakes[10], preserves well-exposed normal and oblique fault systems recording ~3.5 Ma of deformation. Here we integrate ~8,200 geological fault-slip measurements within a hierarchical, multi-scale fault-architecture framework to define the structural boundaries of the IEP and reconstruct principal stress orientations and relative magnitudes from outcrop to crustal scale. The resulting stress architecture reveals a persistent Andersonian tensional regime and a nested, multi-wavelength arcuate organization. At regional scale, stress curvature broadly parallels Moho geometry, whereas shorter-wavelength rotations reflect fault segmentation and structural inheritance. An earlier transtensional stage, immediately preceding the extensional regime, is locally preserved and structurally distinct from the long-lived dip-slip extensional regime that shapes the present seismogenic framework. Independent comparison with focal mechanisms and GNSS-derived strain rates shows strong directional coherence between geological stress indicators over time and ongoing deformation. These observations indicate that geological fault-slip data, when treated within a rigorous multi-scale framework, can reliably contribute to resolve active stress fields substantially extending the temporal window of investigation beyond that accessible from instrumental datasets alone. More broadly, they provide new constraints on stress persistence, scale dependence, and mechanical coherence in intraplate extensional systems, offering a transferable approach for investigating active long-term lithospheric deformation beyond the Italian case study.

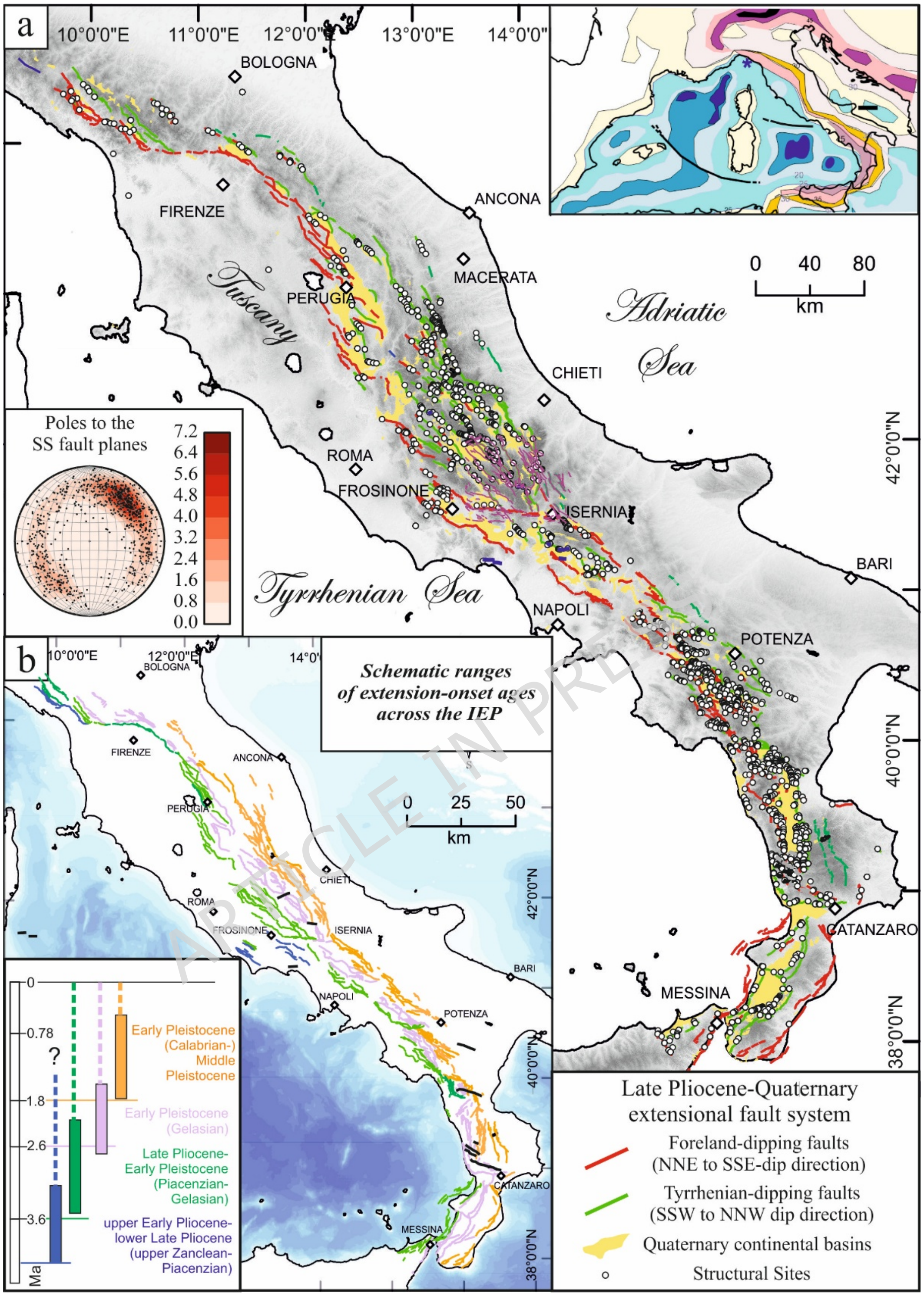

Figure 1. **Structural architecture and spatiotemporal framework of the Intra-Apennine Extensional Province (IEP). (a)** Updated fault traces across the IEP, based on the QUIN 1.0 and 2.0 Host Fault datasets[8,9] and integrated with additional faults compiled from the Geological Map of Italy (1:100,000–1:50,000; https://sgi.isprambiente.it/), the ITHACA database[11] and targeted field surveys, within the broader framework provided by regional geological maps[12,13,14,15,16] (see Methods and Supplementary Fig.1). Structural Sites

from PILOT Datasets 1a and b[17] are shown as open circles (details in Supplementary Fig.2). The upper-right inset shows a schematic Moho-depth map of the Western Mediterranean, with colors indicating increasing crustal thickness from ~5 km to ~45 km. **(b)** Schematic representation of the progressive eastward shift of IEP extensional activity. The length of each coloured bar represents the inferred uncertainty range of fault initiation ages rather than activity duration, whereas dashed lines indicate the possible temporal interval for persistence of activity. Black traces denote isolated faults attributed to a preceding normal–oblique phase[18,19,20,21], Late Miocene–Early Pliocene in age, here referred to as the Early Stage. Maps were originally created by the authors using ArcGIS Pro and refined in CorelDRAW.

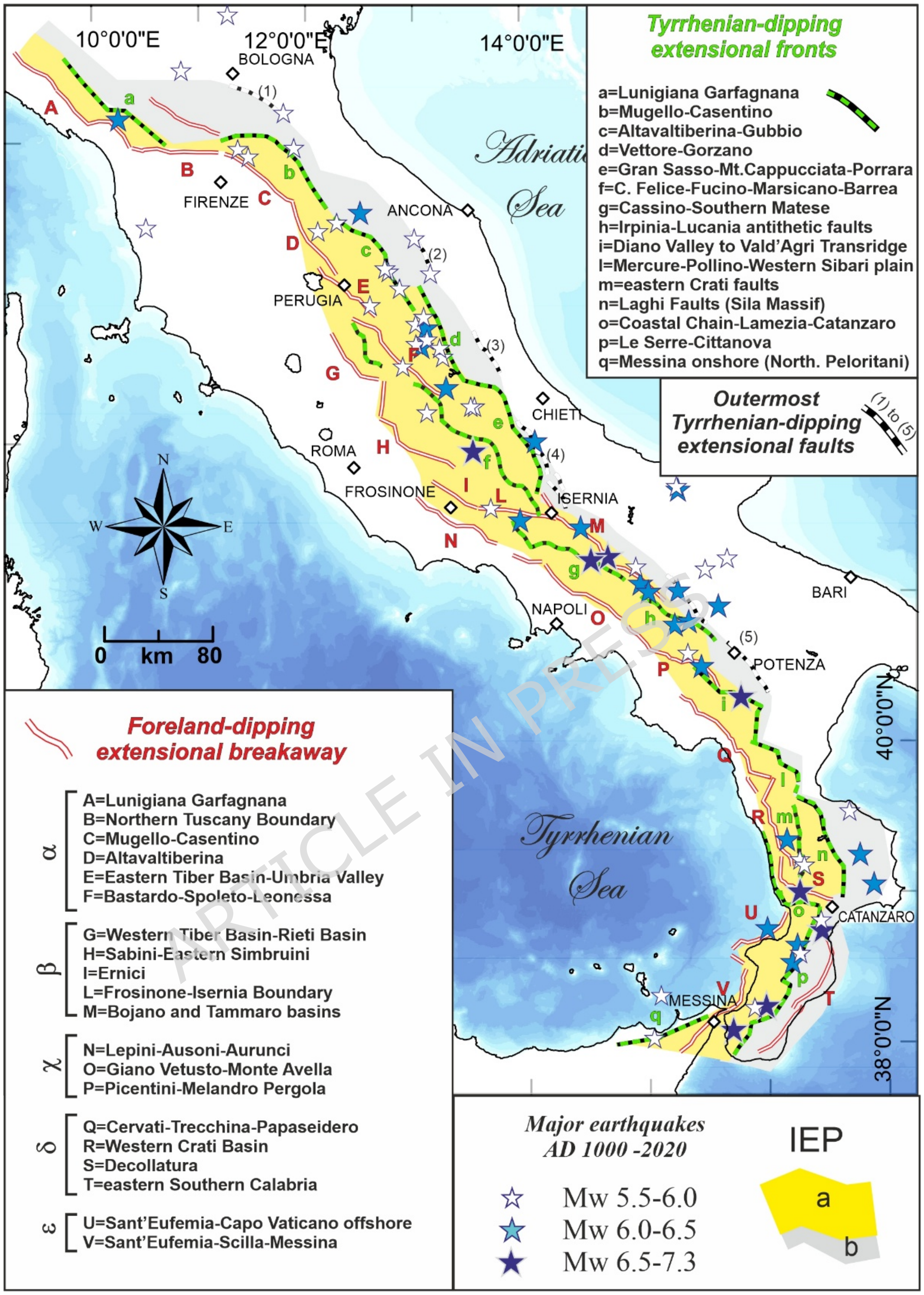

Figure 2. Fault-controlled structural zonation of the IEP. Major longitudinal fault alignments delineate the inner, outer, and outermost structural boundaries of the IEP. Alignments are classified by dip polarity as Tyrrhenian-dipping (dashed green), foreland-dipping (solid red), and outermost Tyrrhenian-dipping (dashed black). Uppercase (A–U) and lowercase (a–p) labels denote neighboring master fault alignments used to envelope the IEP boundaries (see Methods); numbers in brackets (1-5) indicate debated normal faults of the IEP foothills domain (1=Bologna[22], 2=Mt San Vicino[23], 3=Mt dei Fiori[24], 4=Ateleta and

Carovilli-Sassano[25], 5=Potenza-Laurenzana). Five regional foreland-dipping alignments (a – e in the legend) define the internal boundary of the IEP through medium-to-low-angle breakaway traces arranged in a right-lateral en échelon pattern: (a) Etrurian Fault System (*sensu*[26]); (b) Latium–Abruzzi Extensional Detachment (LAED; *sensu*[27]); (c) Southern Latium–Campania east-dipping fault system[28]; (d) Western Northern Calabria–Eastern Southern Calabria foreland-dipping fault system; and (e) Offshore Southern Calabria–Peloritani foreland-dipping fault system (after[29]). The province is subdivided into an inner, well-exposed axial domain (a, yellow) and an outer, largely buried foothills domain (b, gray). Major earthquakes are from Rovida et al.[10]). The map was originally created by the authors using ArcGIS Pro and refined in CorelDRAW.

RESULTS

We reconstruct the stress architecture of the IEP from outcrop to crustal scale through three integrated products developed for this study: (i) the multi-scale PILOT (**P**eninsular **It**a**L**y **O**ver **T**ime) geological stress database[17]; (ii) a tectonic zoning of the province; and (iii) a hybrid geological–seismological–geodetic dataset of tensional directions through time. These products derive from the integration of point-based structural observations (fault-slip measurements to derived principal axes) with linear fault geometries (fault traces) within a structured workflow designed to preserve local kinematic variability while progressively stabilizing stress tensors across increasing spatial scales.

IEP structural framework

The IEP tectonic setting represents the youngest surface expression of the geodynamic evolution that, since the Late Oligocene, has controlled tectonics and magmatism within the Western and Central Mediterranean[30,31,32]. During this evolution, lithospheric stretching developed within the internal domains while coeval compressional belts nucleated along the external sectors, and the overall tectonic system progressively propagated toward the foreland. Positioned east of the thinned Tuscan–Tyrrhenian crustal domain, the IEP forms a ~1000 km-long belt along the Apennine–Peloritani mountain chain[33], crosscutting Late Miocene–Early Pliocene compressional structures (Fig.1). The belt comprises primarily normal and normal-oblique faults of late Pliocene to Present age, with master fault segments dipping either toward the Tyrrhenian hinterland or the Adriatic foreland. Tyrrhenian-dipping faults typically exhibit high-angle geometries (60°±15°), whereas foreland-dipping faults range from low-angle (45°±15°) to high-angle dips[15,26,28].

In this study, the IEP fault pattern is organized into hierarchical structural levels, ranging from fault segments to individual master faults, master-fault alignments, and regional master-fault alignments (see Methods and Figs.1, 2). This hierarchical framework allows recognition of progressively larger and mechanically coherent structural domains and helps identify crustal-scale fault alignments defining a high-resolution structural zoning of the IEP. The IEP inner boundary is defined by enveloping the traces of the five foreland-dipping regional master-fault alignments, arranged in a right-lateral en échelon pattern and marking the internal extensional breakaway of the system (Fig.2). The outer boundary is more complex, reflecting the internal structural variability of the province. The inner IEP axial domain, corresponding to the mountain belt (zone a, yellow in Fig.2), is externally bounded by well-exposed alignments of Quaternary Tyrrhenian-dipping master faults characterized by significant cumulative throw, strong geomorphic expression, and documented seismogenic potential[34]. In contrast, the outer IEP foothills domain (zone b, grey in Fig.2) is bounded by Tyrrhenian-dipping, discontinuous, locally isolated faults distributed within the foothills sectors[22,23,24]. Nevertheless, these faults define a structural alignment consistent with the distribution of extensional seismicity[35,36,37] and with the dilatation geodetic strain[38]. Accordingly, the IEP outer boundary reconstructed here extends farther east than in most seismotectonic zonations of the Apennine extensional domain[34,36].

A key regional feature of the IEP is the systematic eastward rejuvenation of fault activity[14,30,39,40,41,42,43] (Fig.1b). By projecting onto the reconstructed IEP fault system, the available chronological constraints on fault-activity onset[8,9], together with their ranges of variability, we outline a simplified interpretative scheme identifying four partially overlapping longitudinal deformation bands progressively activated eastward at intervals of ~1 Ma (Fig.1b). Within the regional structural framework, a clear and systematic eastward migration pattern emerges. The two innermost alignments (blue–green in Fig.1b) are dominated by foreland-dipping faults, whereas the two outer alignments (pink–orange) are dominated by Tyrrhenian-dipping faults. Deformation is currently concentrated along the two outermost bands, including the foothills fault domain, consistent with the distribution of the largest earthquakes (Fig.2), although low-magnitude extensional seismicity remains widespread[35].

A limited number of broadly south-dipping normal–oblique faults in Latium, Abruzzo, Campania, and Calabria regions do not conform to the longitudinal migration pattern described above (black traces in Fig.1b). Instead, they record an earlier deformation stage that post-dates the Late Miocene–Early Pliocene compressional phase and pre-dates the Late Pliocene–Quaternary extensional regime[18,44]. This subordinate phase, here termed the Early-Stage, represents a temporally and kinematically distinct component within the overall evolution of the IEP. Its recognition is primarily based on cross-cutting relationships and regional kinematic constraints, although the time intervals proposed in the literature partly vary among different sectors of the IEP and among authors[18,19,20,23,24]. These previous studies mainly documented local or sector-scale occurrences of older oblique left-lateral deformation, whereas the present work integrates these observations into a coherent regional reconstruction of the Early-Stage stress architecture across the central and southern Apennines. Accordingly, the term “Early-Stage” is used here in a broad tectono-stratigraphic sense rather than to define a narrowly constrained chronological interval.

Stress architecture across scales

The stress architecture of the IEP is resolved hierarchically from Structural Sites (SS) to Fault Groups (FG) and Fault Supergroups (FSG) through multi-scale inversion of thousands of fault-striation pairs (FSP) integrated within the PILOT stress database[17]. The hierarchical attribution of FSP to SS, FG, and FSG was defined a priori based on both the multi-scale fault architecture of the IEP, reconstructed from mapped host-fault traces and fault-system geometry (Fig.1a), and on the kinematic coherence of deformation-axis patterns already identifiable at SS scale from the literature[8,9]. The PILOT stress inversion was subsequently applied to progressively aggregate datasets after exclusion of kinematically incompatible residual populations. The resulting multi-scale tensors consistently define a coherent tensional stress architecture across progressively increasing spatial scales, rather than independent deformation phases, with the exception of the structurally distinct Early-Stage datasets. Because the FSP population size increases systematically from SS (~10 FSP on average) to FG (~100 FSP) and FSG (~900 FSP), different inversion strategies were adopted: statistical PBT inversion[45] for SS-scale datasets and full-tensor stress inversion[46] for FG and FSG datasets. To distinguish the two outputs, full-tensor principal stresses are denoted σ1–σ3, whereas PBT-derived axes are denoted S1–S3; corresponding horizontal components are indicated as σhmax–σhmin and Shmax–Shmin. Stress tensors were ranked using scale-specific quality criteria for SS and FG/FSG datasets (Supplementary Tab.2a,b), whereas kinematic classes were defined according to the rake-based and plunge-based triangular schemes (Supplementary Tab.3); both approaches are described in the Methods section.

PBT inversion was performed on 841 SS assuming two different fracture angles (θ=30° in PILOT Dataset 1a and θ=45° in PILOT Dataset 1b; see Methods and Supplementary Figs.2,3). Comparison of the resulting principal-axis geometries shows that θ=30° yields the most coherent clustering, with S1 concentrated near-vertical and S3 near-horizontal, thus providing the closest approximation to a vertical–horizontal stress configuration. Dataset 1a is therefore adopted as the reference SS-scale solution. Approximately 65% of SS display near-pure dip-slip extensional kinematics, ~27% normal faulting with minor obliquity, and the remaining sites show normal–strike to strike-normal and strike-slip regimes

(Supplementary Tab.4). Synthetic or antithetic FSP located more than ~500 m from major faults remain broadly coaxial with near-fault tensors but exhibit greater dispersion. A large majority of SS (~96%) record a single dip-slip extensional deformation phase, with slip vectors and Shmin approximately perpendicular (90° ± 30°) to local fault trends. This relationship is particularly evident along L-shaped master faults such as Mt. Martani and Mt. Marsicano (FG 41 and 40 in Fig.5), where slip vector trends are radial to slightly convergent. Even where orientations vary locally within the same segment, slip vectors remain kinematically compatible and cluster around a common stress configuration.

A subordinate group of SS (~4%), mainly localized along approximately E–W–striking south-dipping segments (Early Stage; Fig.1b), preserves two slip-vector families: a later one coaxial with the prevailing IEP dip-slip tensional regime and an earlier one characterized by SE-plunging vectors and nearly N–S–trending S3 axes. The distinction between the two populations is supported by their kinematic incompatibility and, where observable, by cross-cutting relationships. Despite representing only a minor fraction of the dataset, the earlier slip-vector population well defines a kinematically distinct and regionally coherent stress configuration.

When the dominant dip-slip SS population is considered as a whole at the regional scale, an arcuate stress pattern emerges (Fig.3a). Shmax and Shmin define two major domains, the Northern and Southern Arcs, separated by a marked change in orientation within the N110° Transition Zone. Shmin streamlines, obtained by interpolating Shmin orientations onto a regular grid, define a continuous and progressively rotating trajectory field along the IEP, outlining a near-radial pattern relative to its axial trend (Fig.3b). In Calabria, a sharp curvature occurs immediately north of the Eastern and Western Crati Basin FGs (FG 45 and 85 in Fig.5), where Shmax sharply rotates from NNE–SSW to NW–SE. By contrast, across the Catanzaro Strait, the rotation remains progressive rather than abrupt.

Beach-ball representations of SS (Fig.4a) provide a synthetic view of local kinematics and allow direct comparison with seismogenic extensional focal mechanisms (Fig.4b). Along active segments, SS pseudo-focal solutions closely match seismological data; along aseismic segments, they provide reliable geometric proxies for the present-day stress field.

Formal inversion of FG yields 89 full stress tensors, spatially distributed according to the polygons shown in Fig.5. For each FG, inversion was performed separately for the prevailing population of kinematically compatible FSP (PILOT Dataset 2a), and for the residual incompatible FSP (PILOT Dataset 2b), identified a priori through PBT axes analysis. Approximately 80% of prevailing FG tensors exhibit near pure dip-slip extensional kinematics, ~16% show normal faulting with minor obliquity, whereas the remaining FG correspond to normal-strike to strike-normal solutions (Supplementary Tab.4). Residual FG, which represent on average ~16% of the total FSP population, mostly remain within the same or an adjacent kinematic class as the corresponding prevailing tensors. Conversely, angular deviations of σhmin between prevailing and residual tensors display a bimodal distribution, with lower-angle clusters (<30°) more common in the Northern Arc and higher-angle clusters (>60°) more common in the Southern Arc (Supplementary Fig.6 and Tab.5).

Prevailing FG tensors of Dataset 2a are nearly coaxial with SS tensors of Dataset 1a, derived assuming θ=30°, supporting strong kinematic consistency across hierarchical structural scales. Comparison between FG tensors and their constituent SS indicates strong internal coherence, with mean angular deviations of ~5° for principal stress-axis plunges (Supplementary Tab.6). Agreement is particularly robust for σ3, whose plunge differs by only ~1° between SS and corresponding FG tensors. More significant deviations occur along curved, L-shaped master faults, where slip vectors and Shmin rotate progressively along strike at the SS-scale, diverging from shear orientation resolved at the FG scale. These local discrepancies likely reflect geometric perturbations superimposed on the regional stress field.

Along the longitudinal extent of the IEP, dip-slip FG define two arcuate domains of σ3 and σhmin (Supplementary Fig.5), consistent with the SS-scale pattern (Fig.3). In the Northern IEP, σ3 rotates clockwise from NNE–SSW to E–W orientations; in the Southern IEP, it continues toward SE–NW trends. The boundary between these domains runs approximately

E–W between Frosinone and Isernia, mirroring the SS-scale Transition Zone (Fig.3). Residual tensors are generally close to prevailing solutions in the Northern Arc, whereas several Southern Arc FG show marked rotations, locally approaching orthogonality (Supplementary Fig.6). FG tensors classified as Early Stage represent 7 of the 89 FG solutions (Supplementary Tables 1,9). As observed in Figure 6 they display nearly N–S–trending σ3 axes (red-labelled plots ID) and lack arcuate rotation.
Stress-ratio values ($\phi = (\sigma_2 - \sigma_3)/(\sigma_1 - \sigma_3)$) derived from prevailing FG tensors predominantly range between 0.1 and 0.6, with a mean of 0.30 ± 0.15 and 84% of values below 0.5 (Fig.7). In the Ramsay–Lisle triangular diagram (Fig.7b), ϕ values cluster within the strongly prolate to near-triaxial field and, in map view, display a modest but systematic from the Northern to the Southern Arc (Fig.7a). Although the variation in ϕ is limited (Fig.7c), the observed southward increase remains larger than bootstrap uncertainty at the scale of the regional population and defines a spatially coherent gradient rather than random local fluctuations.
Normalized differential stress ($d = (\sigma_1 - \sigma_3) / \max(\sigma_1 - \sigma_3)$) is consistently high (median 0.73 ± 0.13), documenting a strongly deviatoric regime, with values tending to be slightly lower in the Northern Arc and higher in the Southern Arc. The highest two values are observed in the Garfagnana and Western Matese (FGs 24 and 87 in Fig.5).
At crustal scale, the FSP population was aggregated into eight regional FSG corresponding to large spatially coherent tectonic domains distributed along the entire IEP and defined according to its hierarchical structural framework (Fig.8; PILOT Dataset 3). Each FSG integrates multiple kinematically homogeneous FG and spans several hundred to a few thousand km^2. In addition to these spatially defined extensional domains, a ninth FSG was constructed separately to include only the Early Stage FSP population, representing the temporally and kinematically distinct pre-extensional deformation Early-Stage.
Along the IEP extent, all FSG bootstrap stereoplots show a tight clustering of principal stress axes, with steep σ1 and near-horizontal σ3 orientations consistent with a near pure dip-slip tensional tensor (Fig.8). The arcuate σhmin geometry observed at the FG-scale persists at crustal scales and broadly parallels the regional curvature of the Moho surface. The Early-Stage FSG yields a prevailing normal–oblique tensor with near-horizontal σ3 trending N170° and σ2 plunging ~30°
All extensional FSG, except the Tuscan–Emilia Apennine domain, have hosted at least one historical or instrumental earthquake with Mw≥6.5, with the largest magnitudes concentrated in the Molise–Eastern Campania and Southern Calabria–Peloritani Ridge FSG.
Inversion results from the SS, FG, and FSG datasets were further evaluated using the here introduced Andersonian Index (AI; see Methods), defined from the plunge of the intermediate principal stress axis to quantify proximity to Andersonian dip-slip or strike-slip end members. AI increases systematically from SS to FG and FSG (Supplementary Tab.7), indicating progressive reduction of stress-axis obliquity with spatial aggregation. By contrast, residual FG tensors and focal-mechanism solutions display lower AI values.
A selection of FG and FSG stress-tensor parameters, classified as quality rank A and B, according to the criteria reported in Table 2b is provided in Supplementary Table 8, whereas the complete atlas of Fault Group kinematics and formal stress-inversion results is presented in Supplementary Table 9.

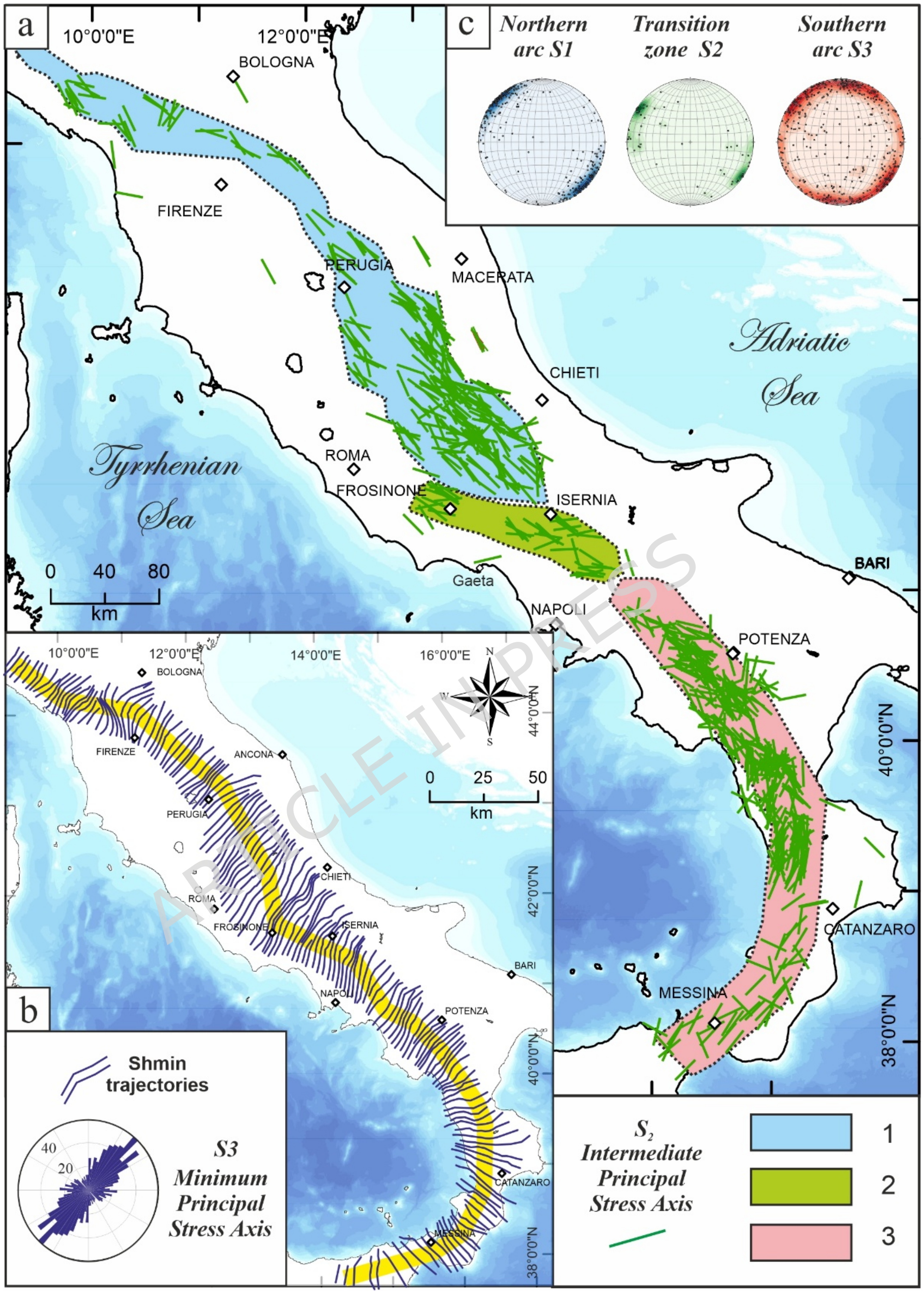

Figure 3. Structural Site-scale stress architecture across the IEP. (a) Maximum horizontal stress (Shmax) orientations derived from SS-scale PBT inversion (θ=30°; Dataset 1a) and corrected following[47]. Colored domains outline the three principal structural sectors of the IEP: Northern arc=1, Transition zone=2, and Southern arc=3. **(b)** Interpolated minimum horizontal stress (Shmin) orientations derived from the same dataset. Shmin trajectories define a continuous arcuate pattern along the IEP axial belt. Rose diagrams

summarize azimuthal distributions of the minimum principal stress axis (S3). The yellow longitudinal polyline follows the IEP axis and is segmented to emphasize major along-strike variations in Shmin orientation. **(c)** Lower-hemisphere stereographic projections of the intermediate principal stress axis (S2) from PILOT Dataset 1a for the Northern arc, Transition zone, and Southern arc sectors, showing the progressive along-strike change in stress-field configuration across the IEP. Maps were originally created by the authors using ArcGIS Pro and refined in CorelDRAW.

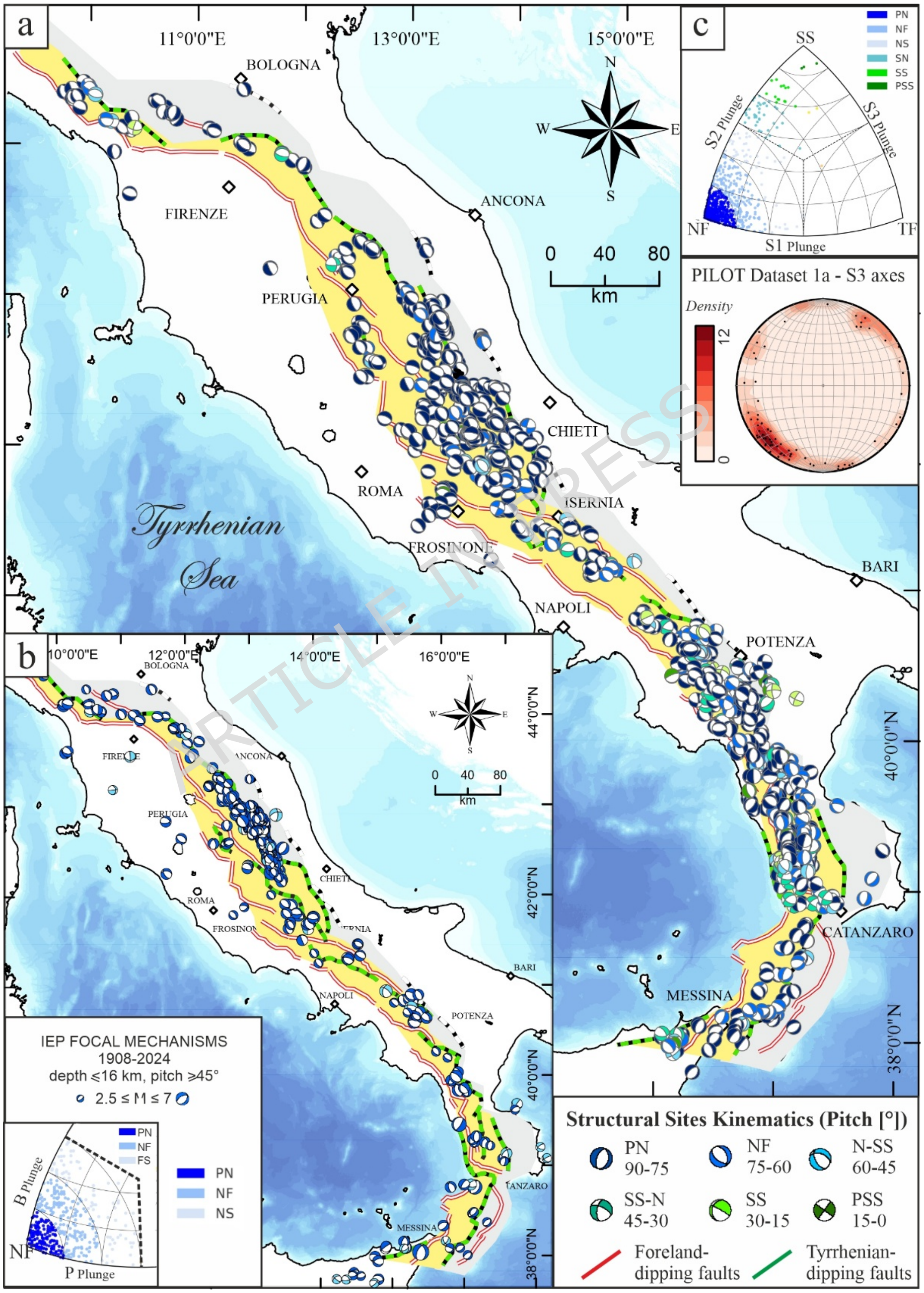

Figure 4. Late Pliocene–Quaternary stress field of the IEP from Structural Sites and instrumental seismicity. **(a)** PBT inversion results from 841 Structural Sites (PILOT Dataset 1a) shown as pseudo–focal mechanisms. Insets display lower-hemisphere (Schmidt) projections of S3 axes and a Kagan[48] ternary diagram of S1–S2–S3 principal stress axes. Beach-balls are colored according to fault kinematics classified by pitch |P|: PN (90–75°, pure normal), NF (75–60°, normal), N-SS (60–45°, normal-strike), SS-N (45–30°, strike-normal), SS (30–15°, strike-slip), and PSS (≤15°, pure strike-slip). Major extensional fault alignments are shown in the background (green=Tyrrhenian-dipping; red=foreland-dipping). **(b)** Earthquake focal mechanisms within the IEP boundaries from RCMT (1908–2014; Mw> 3.8) and TDMT (2015–2024; Mw ≥ 3) at depths ≤16 km, with pure normal (PN) to normal-strike (NS) kinematics shown together with the corresponding Kagan ternary diagram of P, B, and T-axes. **(c)** Kagan[48] ternary diagram of principal stress-axis plunges and lower-hemisphere stereographic projection of S3 orientations for PILOT Dataset 1a[17]. Maps were originally created by the authors using ArcGIS Pro and refined in CorelDRAW.

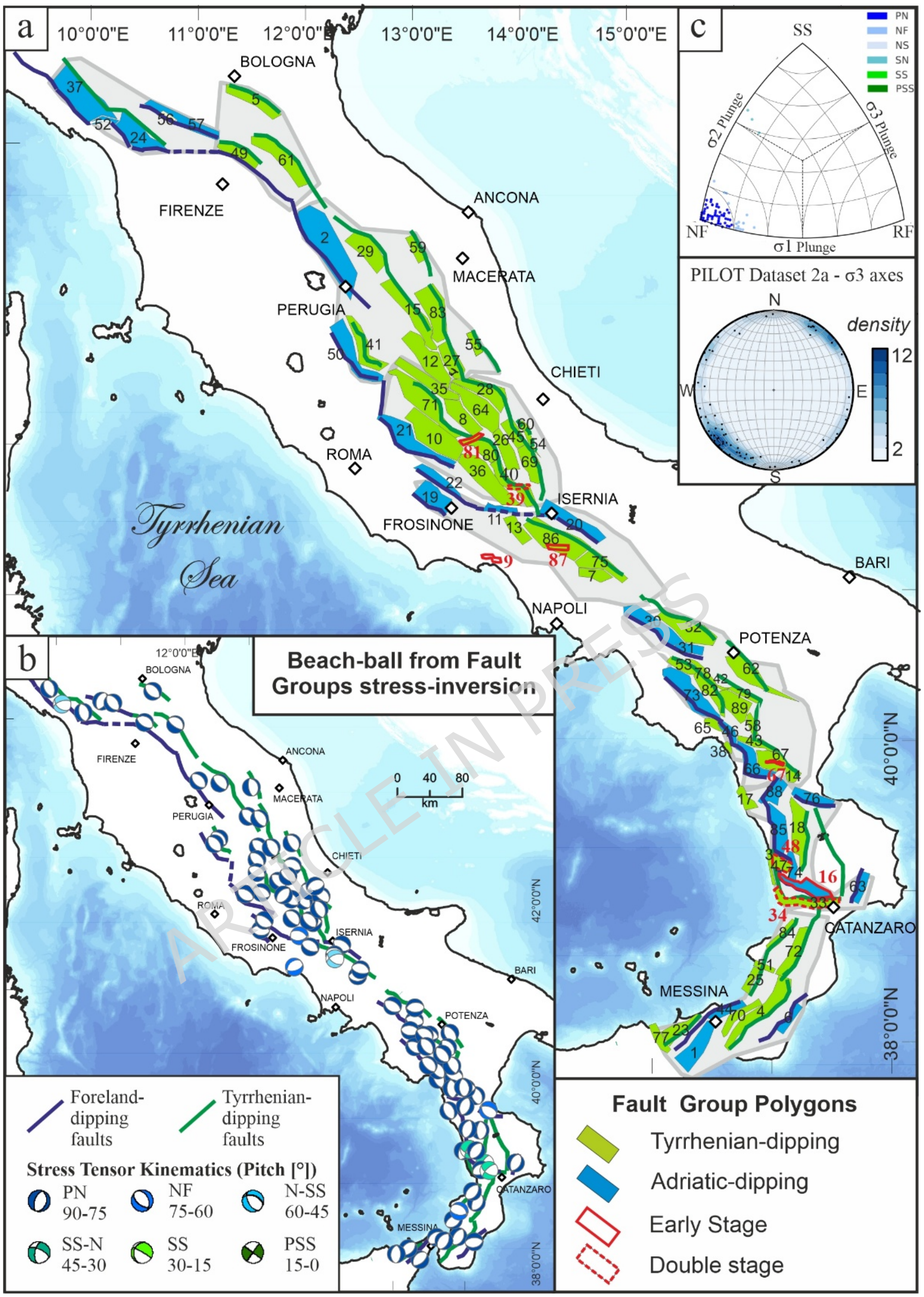

Figure 5. Fault Group-scale structural domains and stress-inversion kinematics (a) Polygons delineating the spatial extent of kinematically homogeneous Fault Groups (FG). Each polygon defines the domain within which a homogeneous stress tensor is computed (PILOT Datasets 2a and b). Coloured fills indicate the predominant fault dip polarity (green=Tyrrhenian-dipping; blue=foreland-dipping). The numerical label within each polygon corresponds to the FG identification number, assigned according to the alphabetical order of FG names; FG names are provided in Supplementary Tables 1b and 9. Fault traces

bounding the polygons are derived from Figs.1 and 2. Red polygon borders highlight FG showing evidence of Early-Stage deformation, as defined in the main text (continuous=exclusively Early Stage; dashed=double-stage evolution). Lowercase red numbers identify Early-Stage FG: 81=Tre Monti; 39=Marsicano (E–W); 9=Campodivivo; 89=Matese; 67=Pollino; 48=Mt. Cocuzzo–Mt. Lucerna; 16=Decollatura; 34=Lamezia–Catanzaro. **(b)** Pseudo–focal mechanism representation of FG kinematics derived from inversion results of PILOT Dataset 2a. **(c)** Kagan[48] ternary diagram of principal stress-axis plunges and lower-hemisphere stereographic projection of σ3 orientations for PILOT Dataset 2a[17]. Maps were originally created by the authors using ArcGIS Pro and refined in CorelDRAW.

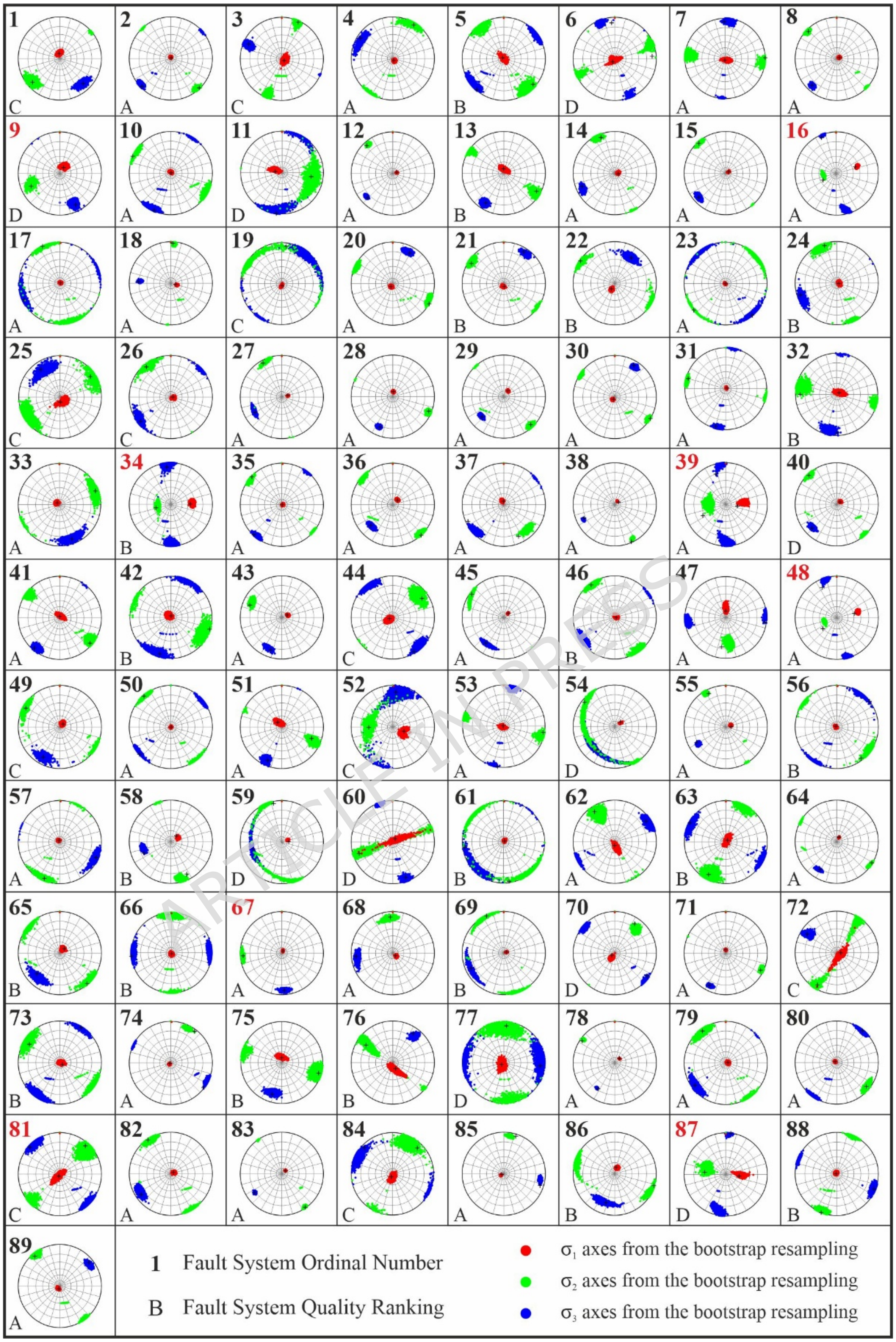

Figure 6. Formal stress inversion of Fault Groups with bootstrap uncertainty assessment. Lower-hemisphere stereographic projections show principal stress axes derived with MSATSI[46] for kinematically homogeneous Fault Groups (FG) of PILOT Dataset 2a[17] (spatial extent in Fig.5). Each panel reports the best-fitting stress tensor (σ_1, σ_2, σ_3;

large symbols) and the 95% confidence regions obtained from 2000 bootstrap resamples (red=σ_1, green=σ_2, blue=σ_3). Panels are numbered consistently with the corresponding FG polygons in Fig.5; red numbers identify Early-Stage FG. Letters A–D indicate the stress-tensor quality ranking, defined according to the threshold parameters reported in Supplementary Tab. 2b.

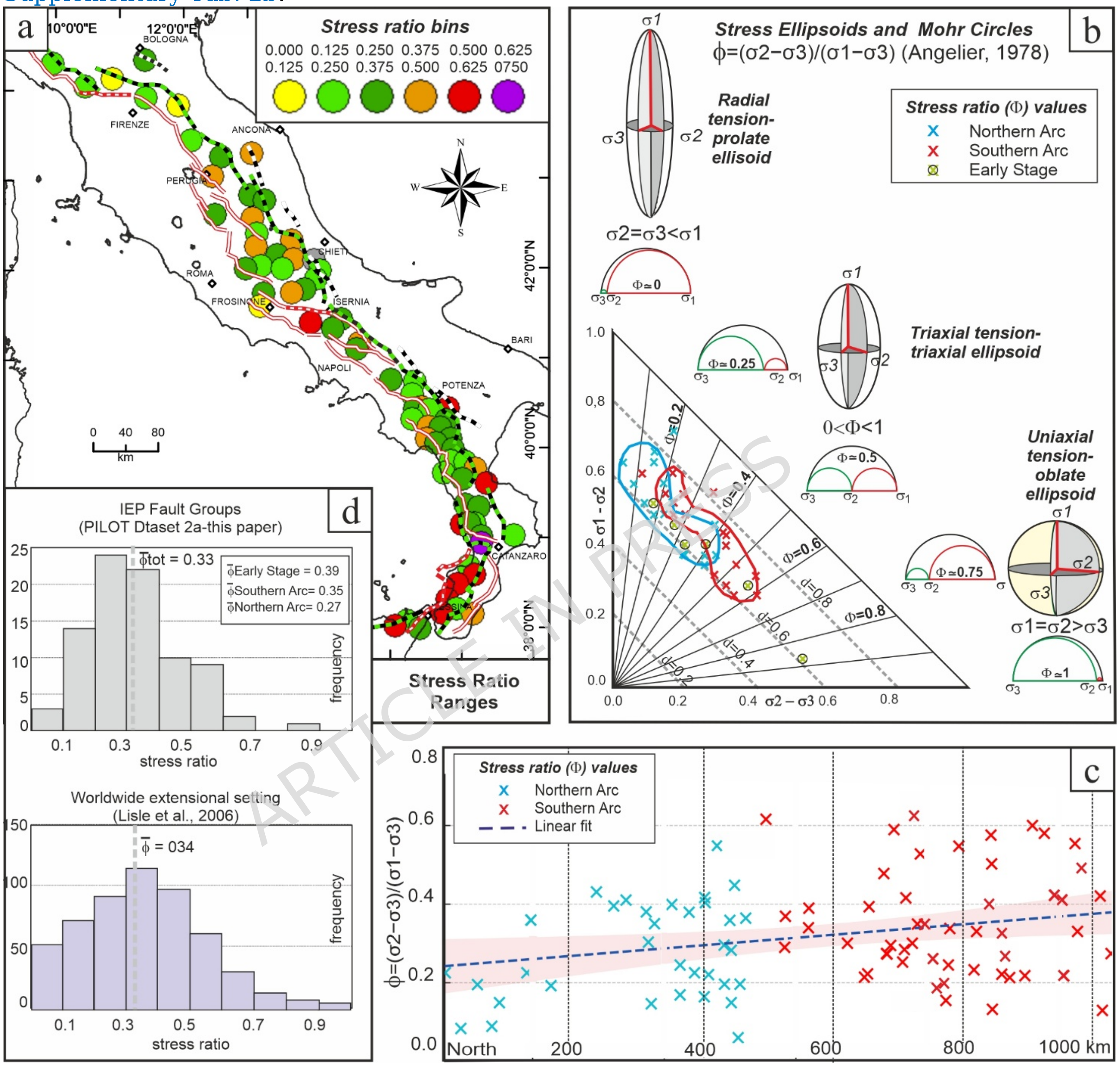

Figure 7. Stress ratio variability and relative differential stress across the IEP. (a) Map of stress-ratio values (ϕ) derived from full-tensor inversions of Fault Groups (PILOT Dataset 2a)[17]. Circles at FG centroids are colored by ϕ bin, where $\phi=(\sigma 2-\sigma 3)/(\sigma 1-\sigma 3)$[49], illustrating along-strike variations in stress-ellipsoid shape. **(b)** Stress tensors plotted on a modified Ramsay and Lisle[50] triangular diagram. Each FG is defined by its shape ratio ϕ and normalized differential stress $d=(\sigma 1-\sigma 3)/\max(\sigma 1-\sigma 3)$. Dashed isolines indicate constant ϕ, and dotted lines indicate constant d. Symbols distinguish Northern Arc, Southern Arc, and Early-Stage domains. Colored contours outline the respective Northern and Southern Arc clusters on either side of the Frosinone–Isernia alignment. **(c)** Scatter plot of ϕ versus cumulative distance (km) along the longitudinal transect shown in Fig.3b. The pink band

represents the ordinary least-squares regression (95% confidence band), indicating a weak positive trend (slope=0.135 ϕ per 1,000 km; R^2=0.070; p=0.0149). D-ranked FG and the extreme outlier FG 60 (ϕ= 0.90) are excluded. **(d)** Histograms of ϕ values for PILOT FG (Dataset 2a)[17] compared with global extensional datasets[51]. Dashed lines mark mean values. The map was originally created by the authors using ArcGIS Pro and refined in CorelDRAW.

Independent validation of stress field continuity over time and the T-hybrid map

The PILOT multi-scale tensors document a coherent tensional stress architecture persisting for at least ~3.5 Ma across the progressively eastward-rejuvenating extensional alignments of the IEP following the onset of the Andersonian regime. To assess whether this stress architecture also persists into the present-day deformation field, Shmin trends from PILOT Dataset 1a (SS scale) were compared with two independent datasets: T-axes from earthquake focal mechanisms[36,37] (Supplementary Figs.7) and horizontal extensional strain axes (εhmax) derived from GNSS velocities[52] (Supplementary Figs.8-9-10).

The geodetic strain-rate field delineates a ~50 km-wide extensional band closely aligned with the IEP (Fig.9b). This band broadly follows the main topographic highs and the Adriatic–Tyrrhenian drainage divide[53] and is largely confined within the mapped innermost and outermost structural boundaries of the IEP (Fig.2). Strain rates range between 25 and 50 nanostrain/yr, with local peaks reaching ~70 nanostrain/yr. The extensional signal is continuous from northern Marche through Abruzzo and Campania and reappears in northeastern and southern Calabria and northeastern Sicily. Corresponding horizontal velocities average ~2 mm/yr and locally exceed ~3 mm/yr[52].

A key feature of the geodetic field across peninsular Italy is an eastward shift of ~50 km in the locus of maximum strain south of the Frosinone–Isernia boundary (Fig.9). Although not previously emphasized, this shift is also evident in declustered seismicity patterns and wavelet-based strain-rate analyses[38]. At first order, εhmax directions reproduce the arcuate geometry of the IEP, rotating from SSW–NNE in the north to WNW–ESE in Calabria and NNW–SSE in the Peloritani sector. However, they do not fully resolve the distinction between the Northern and Southern arcs identified in the geological stress field (Fig.3). By contrast, focal-mechanism T-axes better capture the rotation toward NNE–SSW within the Transition Zone at the northern boundary of the Southern Arc (Figs.3,8,9 and Supplementary Tab.10).

Angular differences among average directions independently derived from SS data, focal mechanisms, and geodetic strain were quantified on a common 10×10 km grid covering the IEP and adjacent areas (PILOT Dataset 4; Fig.9). At each grid cell, the circular mean of the available datasets defines the T-hybrid axis trend, whereas the angular spread (Δ) measures the inter-dataset directional divergence (Fig.9a).

The Δ distribution is skewed toward low values: 50.7% of grid cells show Δ≤10°, and 82.6% fall within Δ≤20°. Only 10.5% of cells range between 20° and 30°, and 6.9% exceed 30°. Larger spreads cluster mainly near the outer IEP margins, along the 41st-parallel discontinuity, and in northern Calabria, indicating transitional strain regimes, locally enhanced structural complexity, and/or reduced data resolution.

The T-hybrid map therefore provides a spatially continuous representation of the IEP extensional field through integration of complementary datasets sampling different temporal windows, bridging long-term geological deformation with seismological and geodetic observations of present-day tectonic processes[54].

Comparison of independent geological, seismological and geodetic tensional/extensional axes within each FSG (Supplementary Tab.10) indicates generally small directional differences, with most FSG showing maximum angular deviations below 20° and only the Southern Latium-Molise-Northern Campania Apennine FSG reaching ~28°.

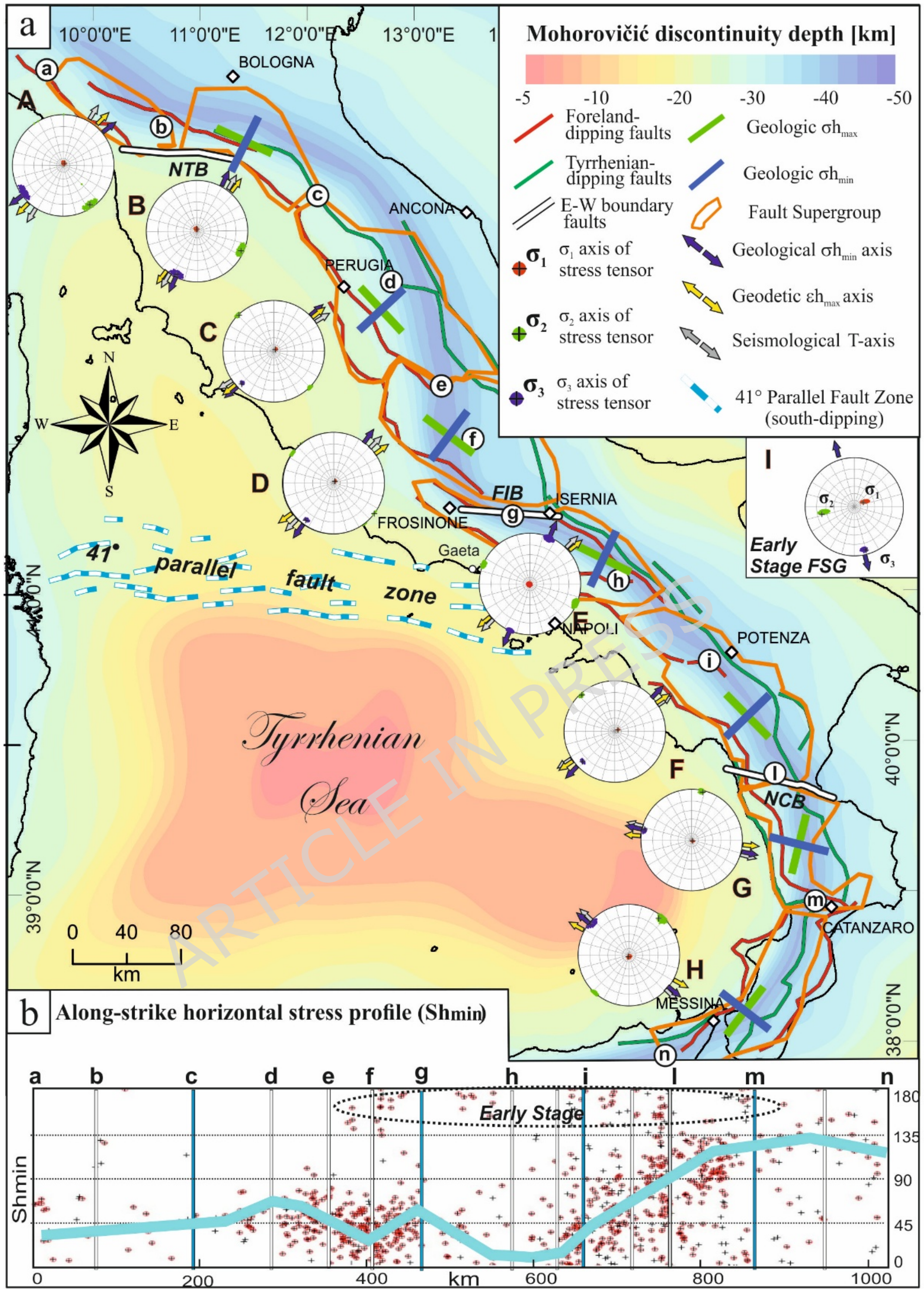

Figure 8. IEP crustal-scale stress architecture. (a) Moho depth map compiled from the EPcrust 2.0 model[55], regional receiver-function datasets[42], and legacy isodepth contours derived from seismic-refraction profiles[56,57,58]. Major structural boundaries described in the main text are shown, including the 41° Parallel Fault Zone and three E–W fault systems (NTB=Northern Tuscany Boundary; FIB=Frosinone–Isernia Boundary; NCB=Northern Calabria Boundary). Orange polygonal lines delineate the eight spatial FSGs (A=Liguria-Tuscan Apennine, B-Tuscan-Emilia Ap., C=Latium-Abruzzo Ap., E=Molise-Eastern Campania Ap., G=Northern and Central Calabria Ridge, H=Southern Calabria-Peloritani Ridge).

Stereoplots A–I display principal stress axes for each FSG with 95% bootstrap confidence regions (PILOT Dataset 3)[17]; the arrows indicate mean geological Shmin, geodetic εhmax, and seismological T-axes (PILOT Dataset 4)[17]. **(b)** Longitudinal Shmin profile from PILOT Dataset 1a[17] (red dots), projected along the longitudinal transect shown in Fig.3b. Lowercase letters (a–n) mark projection intervals corresponding to major along-strike changes in stress orientation. The smoothed Shmin trend highlights multi-wavelength variations of the horizontal stress field along the IEP. The map was originally created by the authors using ArcGIS Pro, Move (Petex ltd) and refined in CorelDRAW.

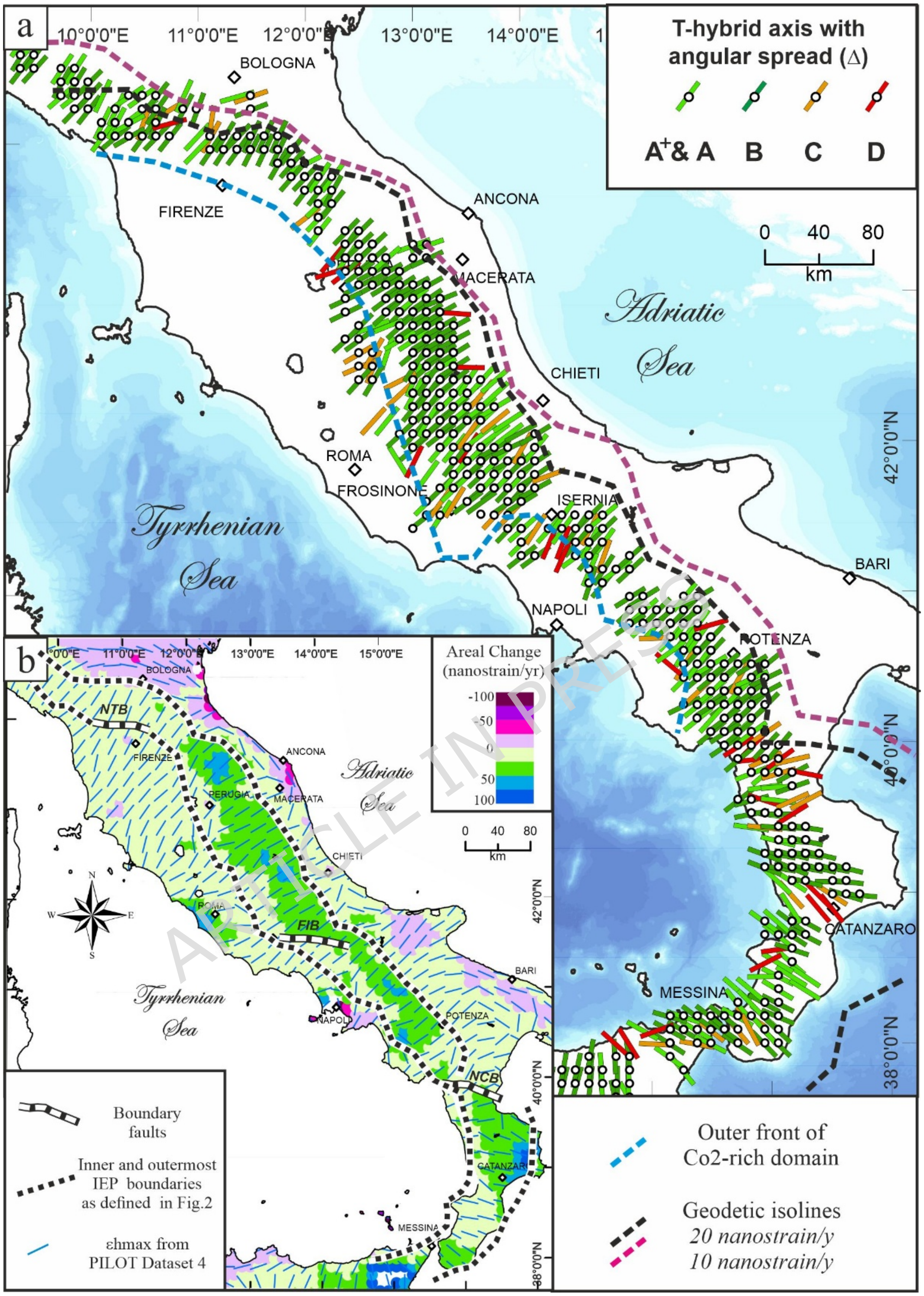

Figure 9 - Hybrid tensional architecture of the IEP and geodetic dilatation strain rate. (a) Gridded T-hybrid axes from PILOT Dataset 4[17], representing the integrated horizontal tension/extension pattern across the IEP. Hybrid orientations are derived from the combination of (i) Shmin axes from Structural Sites (PILOT Dataset 1a)[17], (ii) T-axes from earthquake focal mechanisms, and (iii) εhmax axes from the geodetic strain-rate field, representing the greatest horizontal extensional strain rate. Tensional orientations were

computed using the Stress2Grid algorithm[59]. Bar colours indicate the quality class of each T-hybrid solution (A+ to D) as defined in the Methods, reflecting angular spread (Δ) and the number of contributing datasets. Dashed isolines indicate isolines at 10 and 20 nanostrain/yr of dilatation strain rate, delineating the main geodetic extensional band. The light-blue dashed line marks the outer front of the CO_2-rich domain[60]. **(b)** Geodetic strain-rate field derived from the horizontal GNSS velocity field of Serpelloni et al.[52], interpolated using VISR[61]. Colors represent dilatation (nanostrain/yr). Major near E–W boundary faults (NTB, FIB, NCB) are shown as in Fig.8. Black dashed lines indicate the inner and outermost IEP structural boundaries defined in Fig.2. Maps were originally created by the authors using ArcGIS Pro and refined in CorelDRAW.

DISCUSSION

Geomechanical insights

Whether brittle deformation in the upper crust conforms to strict Andersonian stress conditions remains debated[62,63]. The reconstructed multi-scale stress architecture of the IEP provides an empirical test of this issue across spatial scales within an intracontinental context. The progressive tightening of S1 toward near-vertical plunges and of S3 toward near-horizontal orientations in the SS inversion, especially when assuming θ=30°, together with the near-coaxial coherence between SS-, FG-, and FSG-derived tensors (Datasets 1a, 2a and 3), demonstrates that the vertical–horizontal stress geometry is not imposed by methodological assumptions but represents a robust property of the IEP regional stress field. The systematic increase from SS to FG and FSG of the here-defined Andersonian Index (AI, Supplementary Tab.7) further indicates that local obliquity diminishes as spatial aggregation increases, implying that second-order perturbations are superimposed on a first-order tensional framework. Accordingly, the progressive stabilization of stress tensors with increasing spatial aggregation supports the interpretation that SS, FG, and FSG represent different structural expressions of the same first-order tensional stress field rather than unrelated deformation phases. Importantly, AI quantifies geometric proximity to Andersonian end-member configurations based on the plunge of σ2 and does not, by itself, imply a specific kinematic regime unless accompanied by the corresponding horizontal arrangement of σ2 and σ3. Departures from this configuration are spatially organized rather than random. Along curved master faults, particularly those with L-shaped geometries, both slip vectors and minimum horizontal stress orientations rotate progressively along strike, locally diverging by up to ±30° from the shear direction predicted by regional tensors. These rotations likely reflect geometric stress refraction associated with fault curvature, segmentation, or variations in mechanical connectivity.

The observed short-wavelength variability implies that FG-scale tensors, while representative of average regional conditions, may not adequately resolve slip tendency or rupture potential at the scale of individual fault segments. Outcrop-scale tensors are necessary to provide a more reliable basis for evaluating local mechanical conditions. Comparable behaviour at a larger scale has been documented along major plate-boundary faults such as the San Andreas and the Great Sumatran fault systems, where pronounced bends induce local stress reorientation while the first-order regional stress regime remains stable[4].

Stress ratio (ϕ) values across the IEP are predominantly low to moderate (0.1–0.6) and display a modest southward increase from the Northern to the Southern Arc (Fig.7a). This trend corresponds to a progressive transition from strongly prolate toward near-triaxial configurations (Fig.7b), without approaching fully oblate geometries capable of promoting systematic σ_1–σ_2 interchange or dominant strike-slip regimes. The observed increase in triaxiality within the Southern Arc spatially correlates with regional variations in crustal architecture and thermal structure, including greater crustal thickness[42,55,56,57,58] and comparatively lower heat flow[64]. This is consistent with interpretations proposed for segmented extensional systems and rheologically heterogeneous lithosphere in both the Mediterranean region and other extensional provinces[24,65,66,67]. Although a quantitative assessment of these rheological and thermal controls lies beyond the scope of the present study, the stress architecture reconstructed here provides a potential framework for future integration of geological stress inversion with independent constraints on lithospheric structure, rheology, and thermo-mechanical evolution.

Normalized differential stress derived from FG tensors remains systematically high (Fig.6b), suggesting persistently elevated deviatoric conditions and proximity to frictional failure over geological timescales. This sustained deviatoric state is consistent with near-critical stress models for extended continental crust[68]. The coexistence of elevated differential stress and stable Andersonian geometry suggests that the IEP forms a mechanically coherent extensional system capable of accommodating long-term loading without large-scale stress reorganization.

Independent inversion of residual FG populations (Dataset 2b) provides important constraints on the extent of local variability within the regional stress field (Supplementary Fig.6; Supplementary Tab.5). The observation that approximately 82% of the residual FG tensors remain within the same or adjacent kinematic class as the corresponding prevailing tensor indicates that, across most of the IEP, inclusion of incompatible FSP does not substantially modify the first-order dip-slip tensional regime resolved at FG scale. Larger σhmin rotations, more frequent in the Southern Arc, likely reflect enhanced segmentation, inherited structural geometries, and/or localized mechanical heterogeneity. Bootstrap solutions from residual FG occasionally approach local σ_2–σ_3 interchange; however, these cases reflect localized tensor uncertainty rather than systematic reorganization of the regional stress field.

Tectono-geodynamic interpretation

The persistence of the mechanically coherent stress architecture described above also provides constraints on the lithospheric-scale processes governing extension. Shmin trajectories derived from SS are largely perpendicular to crustal-thickness gradients, and FG-scale tensors indicate near-pure dip-slip kinematics with σ_3 azimuths rotating radially along the Northern and Southern arcs (Figs.3,5,8). In agreement with recent studies on the Apennine topographic and lithospheric architecture[32,42] such arcuate stress field architecture likely reflects the superposition of processes operating at different spatial wavelengths, including deep lithospheric forcing, residual topography, fault segmentation, structural inheritance, and local topographic perturbations. Although this spatial correspondence does not imply a direct one-to-one mechanical control by Moho geometry, it indicates that crustal-thickness gradients and inherited lithospheric structure likely contribute to the large-scale organization of the IEP tensional stress field.

At several locations, radial rotation of σ_3 and bending of fault traces coincide with sharp eastward shifts of the extensional front. These shifts, constrained by integrated stress, structural, geodetic, and tomographic data, are identified along three major E–W alignments: the Northern Tuscany Boundary (NTB), the Frosinone–Isernia Boundary (FIB), and the Northern Calabria Boundary (NCB; Figs.8,9).

The NTB is clearly expressed by the sharp eastward stepping of the east-dipping extensional breakaway along the inner IEP boundary between the Lunigiana–Garfagnana and Mugello–Casentino FG17 (24 and 49 in Fig.5). It is partially mirrored in the geodetic dilation field by coherent bending of the belt of maximum extensional strain (Fig.9b).

The FIB bounds the Southern Arc to the north, where stress axes rotate toward NNE–SSW within the Transition Zone; its crustal significance is reinforced by seismic tomography imaging of an E–W low-attenuation corridor[69] and by structural evidence of N–S tension along the same alignment[27,70]. The geodetic dilation field also displays a marked eastward shift of the main extensional belt across the same alignment (Fig.9b). The FIB lies slightly north of the onshore continuation of the 41st Parallel Fault Zone (Fig.8), an inherited lithospheric discontinuity separating the northern Tyrrhenian thinned domain from the southern ultra-thinned sector[30,57]. Its eastern termination reaches the Gaeta Gulf[24,71], and remains broadly parallel to the FIB trend although slightly shifted southward (Fig. 8). During the Early Pliocene, the 41st Parallel Fault Zone may have accommodated oblique lithospheric-scale extension, through reactivation of an inherited transcurrent lineament of the Apennine compressional system[24,30,57,71]. In Late Pliocene–Pleistocene times, it may have contributed to controlling the arcuate shape of the Moho beneath the Southern Arc and the nucleation of WNW–ESE-trending fault structures within the Transition Zone.

The NCB bounds the Calabria metamorphic arc to the north and corresponds to a marked rotation of Shmin from SW–NE north of the boundary to WNW–ESE south of it. This sharp directional change is consistently expressed in both the SS- and FSG-derived stress maps (Figs.3,8) and is also marked in the geodetic dilation field by an abrupt eastward shift of the extensional domain (Fig.9b).

Within this architecture, the double-arc geometry of the IEP stress field is best interpreted as a primary tectonic feature developed in spatial and kinematic coherence with inherited lithospheric discontinuities rather than as a secondary oroclinal bending[72]. Independent evidence from receiver functions, thermochronology, and drainage-divide migration[42] converges toward this interpretation. These results challenge models that interpret IEP faults as shallow structures reactivating inherited thrusts[73,74,75] and instead support scenarios in which arcuate fault systems reflect deep-seated anisotropies or basal tractions[76]. The absence of evidence for transversal NE–SW discontinuities dissecting the Apennines[77], or for an active tear fault across the Catanzaro Strait[78,79,80], further supports distributed deformation within a coherent arcuate system. Similarly, interpretations invoking an active Pollino strike-slip fault, accommodating slab retreat[81], are not supported by stress inversion results; E–W oblique structures correspond to the Early-Stage deformation and predate the current Andersonian regime.

The IEP crustal-scale coherence is expressed geometrically through a nested hierarchy of stress wavelengths that progressively modulate the regional arcuate pattern.

Integration of SS-, FG-, and FSG-scale orientations reveals five characteristic wavelengths, partly illustrated by the IEP along-strike Shmin profile of Figure 8b. At first order (~1000 km), the entire IEP arc from Tuscany to northeastern Sicily shows progressive rotation of stress axes. At second order (~400–500 km), the Northern and Southern arcs define the principal convex geometries. Third-order wavelengths (~50–100 km) correspond to curvature associated with major fault systems, including the Calabrian Arc, here interpreted as a subordinate curvature embedded within the broader Southern IEP arc. Fourth-order wavelengths (~10–30 km) reflect along-strike rotations within individual master faults, while fifth-order (<10 km) variations capture local stress perturbations, commonly linked to inherited structures acting as seismological barriers[82]. These short-wavelength perturbations likely reflect the influence of fault bending, segmentation, local topographic effects, and structural inheritance superimposed on the first-order regional stress architecture.

This hierarchy aligns with the World Stress Map framework[2], in which first-order patterns define intraplate stress provinces and shorter wavelengths reflect tectonic gradients and fault-scale complexity. Comparable arcuate stress–fault architectures are documented in other extensional systems, including the Basin and Range[1], the Aegean[65], the Pannonian Basin[83], the Alboran Domain[66], and the South China Sea[84], all characterized by pronounced crustal anisotropy or Moho curvature.

The IEP, therefore, represents a case in which large-scale arcuate geometry is progressively modulated by intermediate and local structural controls without disrupting regional extensional coherence.

The IEP represents the youngest and currently active extensional phase within a long-lived deformation sequence that, since the Middle Miocene, has driven progressive stretching of the Tyrrhenian lithospheric domain in the rear of the Apennine-Maghrebide orogenic belt[30,31,32]. During an overall time span of ~12–13 Ma, four major extension–compression couples developed through distinct regional tectonic episodes[43], spaced by ~3–4 Ma in initiation age and by ~50–100 km in their eastward spatial migration[85]. Consequently, the inferred long-term rate of the eastward stepping of the extensional domain is on the order of a few centimetres per year (~1.5-3.0 cm/yr). This value is approximately one order of magnitude greater than the cumulative slip rates of the extensional fault alignments within the present IEP, which are generally on the order of a few millimetres per year (≈2–3 mm/yr;[86,87]). This configuration suggests that the evolution of the overall Apennine extensional system primarily reflects discrete eastward jumps of first-order extensional domains through time, superimposed on comparatively slower strain accumulation within each individual domain.

Within this long-term evolutionary framework, the evidence for the Early-Stage stress field outlined here, although representing only ~4% of the overall PILOT stress data, is especially significant. Across scales, the Early Stage FSP population records a regionally coherent left-lateral transtensional deformation sparsely distributed across Central and Southern Italy along south-dipping faults, fundamentally distinct from the radially organized Late Pliocene–Quaternary stress field. Although expressed through relatively discontinuous and spatially scattered structures, these features may reflect distributed reactivation of inherited lithospheric anisotropies accommodating eastward block translation under dominant basal shear transmitted from the already thinned inner Tuscan–Tyrrhenian toward the still-thickened crust of the IEP. Since the Late Pliocene, deformation evolved into near-pure dip-slip Andersonian extension, with σ_3 progressively adopting a radial geometry approximately perpendicular to crustal-thickness gradients and Moho curvature, indicating increasing control by differential gravitational potential energy[42] and consistently with numerical models linking stress rotation to mantle flow and lithospheric-thickness contrasts[88].

Geodynamic models frame the Apennine extension as the surface expression of torque balance among basal shear, lithostatic gradients, and lateral resistance[89]. Within this framework, each major extensional phase may evolve through three successive stages: (1) an initial transtensional stage driven by eastward basal drag; (2) a mature Andersonian stage characterized by radially organized σ_3 and outward-shifting deformation bands, consistent with numerical models linking stress rotation to mantle flow and lithospheric-thickness contrasts[88]; and (3) a lithospheric stretching stage involving progressive attenuation and nucleation of a new extensional front farther east.

Within the present IEP, relic E-W Early-Stage structures preserve evidence of the initial transtensional configuration, whereas the arcuate system represents the dominant near-pure extensional stage also governing present-day IEP deformation and seismic hazard.

Over the last ~3–3.5 Ma, the IEP evolved through progressive eastward growth of partially overlapping and broadly coaxial longitudinal fault bands (Fig.1b), while the regional stress field progressively acquired its present double-arc geometry (Figs.3,8). The present IEP may therefore represent an advanced stage of the mature Andersonian extensional cycle, potentially preceding a further stepwise eastward migration of extension into and beyond the Apennine foothills.

In the context of this long-term evolution, the major E–W alignments (i.e., NTB, FIB, and NCB) may have experienced different kinematic roles through time, evolving from left-lateral transtensional discontinuities during the Early-Stage into right-lateral transtensional transfer structures kinematically compatible with the arcuate Andersonian extensional regime, characterized by progressively rotating σ_3 trajectories from SSW–NNE to WSW–ENE..

Conceptual implications for stress-field continuity

A central issue in active tectonics concerns how to define and interpret the present-day stress field within a long-term geological framework. Methodologically, this involves the extent to which geological, geodetic, and seismological datasets can be integrated into a coherent representation of crustal deformation. Semantically, it also concerns the meaning of terms such as “paleo-stress” and “active stress”, often used inconsistently across disciplines. We advocate an integrative perspective that emphasizes tectonic continuity rather than rigid temporal thresholds and adopts terminology grounded in mechanical coherence rather than chronology alone.

Stress and strain are distinct quantities: stress is force-based, strain displacement-based. Under homogeneous tectonic conditions, however, their tensors may be coaxial, with opposite orientations of maximum and minimum principal axes. Accordingly, stress-derived tensional axes (σ_3, σhmin) and strain-derived extensional axes (ε_1, εhmax) provide complementary views of the same deformation process.

The comparison between geological stress indicators from the IEP, integrated over ~3.5 Ma, and present-day GNSS-derived strain rates is based on the commonly adopted approximation that, under persistent tectonic conditions, principal stress and strain-rate tensors remain approximately coaxial over geological timescales[2,90]. Minimum principal stress orientations (σhmin) are therefore expected to be broadly parallel to maximum extensional strain-rate directions (εhmax). Within this framework, the comparison is restricted to tensor orientations rather than stress or strain magnitudes. In the present study, the directional agreement among geological minimum principal stress orientations, focal-mechanism T-axes, and geodetic strain-rate directions (Fig.9) is in any case not assumed a priori, but emerges independently from the results, supporting the long-term persistence of the regional tensional stress field.
In the Apennines, other studies document strong directional agreement between geodetic strain and earthquake focal mechanisms, supporting εhmax as a reasonable proxy for seismogenic tensional stress[38,91]. Additional works report substantial agreement between field-observed fault kinematics and GPS-based modelling[92,93]. From a structural-geology perspective, however, field-based stress tensors remain essential for bridging spatial and temporal gaps, especially in regions with sparse instrumental seismicity or uneven GNSS coverage.

Here we integrate geological, seismological, and geodetic datasets into a gridded hybrid T-axis map for the IEP (PILOT Dataset 4)[17]. Within each grid cell, compatible directional indicators from multiple sources are averaged into a single orientation, the T-hybrid axis, accompanied by its angular dispersion (Δ). Pairwise angular comparisons and misfit distribution (Supplementary Figs.9-10) together with Δ distributions from the integrated T-hybrid field (Fig.9a) provide a quantitative assessment of multi-source internal coherence. Across the IEP, geological Shmin orientations display high local variability, focal-mechanism T-axes define coherent regional trends, and GNSS-derived εhmax produces a smoother, spatially continuous strain field. While GNSS data ensure regional coverage, they may smooth fault-scale features. For example, geodetic strain reproduces the first-order arcuate geometry of the IEP but does not resolve the NNE–SSW rotation within the Transition Zone, which is clearly captured by geological and seismological datasets (Fig.3).

Large angular spreads (Δ>30°), observed in only 7% of grid cells, should not be interpreted solely as poor data quality. They may instead mark zones of stress reorganization, evolving fault interaction, or limited spatial resolution. In the T-hybrid map, the largest Δ values cluster near the outer IEP margins, along the Frosinone-Isernia Boundary, and in northern Calabria, suggesting transitional strain regimes and/or locally reduced data density.

The conceptual implications of the T-hybrid map extend beyond the methodological aspects of multi-source data integration and bear directly on the definition of long-lasting stress fields persisting into the present-day tectonic regime. The term “paleostress” is problematic when applied to stress records that remain mechanically compatible with the present regime. Conversely, the term “active” lacks a uniform definition: some authors restrict it to post–Last Glacial Maximum activity (~20 ka in Italy[94]); others extend it to the Late Pleistocene[95]; others apply it to the overall time span of a persistent stress field[8,9,96]. In the IEP, the dip-slip tensional stress regime has persisted for ~3.5Ma, progressively propagating and expanding outward. This persistence does not imply strict temporal invariance at shorter timescales, but rather the absence of first-order regional stress reorganization during the progressive eastward migration of the IEP internal extensional front. In fact, the four longitudinal deformation bands identified across the IEP, despite their progressively younger onset ages (~1Ma apart; Fig.1b), display consistent dip-slip extensional kinematics and near-coaxial Shmin orientations, and therefore do not define distinct stress domains through time. Moreover, the spatial continuity and progressive rotation of Shmin trajectories along strike (Fig.3b) argue against intermediate regional-scale stress rotations. Together, these observations indicate that successive eastward rejuvenation of deformation within the IEP occurred within a mechanically stable first-order stress framework, upon which only second-order, fault-scale perturbations were superimposed.

Comparable persistence is documented in other intraplate settings, such as the western United States, where stress orientations remained stable over much longer time intervals, up to 10Ma[67]. Long-term geological stress indicators compatible with present-day stress are incorporated in the World Stress Map[2], under the assumption that faults lacking recent surface rupture may remain seismogenic if favourably oriented within the current stress field, a criterion adopted by institutions such as USGS and SCEC, and fully supported by the PILOT results presented here. Within this framework, we propose reserving "paleostress" for fossil stress fields no longer compatible with the present regime, such as the Early-Stage one identified here. For geological stress records aligned with the ongoing deformation regime, including the dip-slip normal faults of the IEP, we propose the term "active stress over time", emphasizing mechanical persistence across geological stages. Similarly, faults lacking Late Pleistocene–Holocene displacement but mechanically compatible with neighbouring active segments should be described as "potentially seismogenic". This terminology foregrounds tectonic continuity, acknowledges preservation limits, and prioritizes mechanical compatibility over rupture recency, thereby strengthening the role of geological stress datasets in seismotectonic interpretation and hazard analysis.

CONCLUSIONS

This study presents the first high-resolution geological reconstruction of a multi-wavelength stress field through time across the Intra-Apennine Extensional Province (IEP), based on uniquely large multi-scale fault-slip dataset analysed in strict association with mapped host faults at the scale of the entire Italian extensional belt. The results document a long-lived and still active tensional stress regime that, since at least Late Pliocene times, has governed the development of the current arcuate belt, characterized by predominantly dip-slip kinematics and potentially seismogenic structures. This regime was locally preceded by a subordinate left-lateral transtensional stage and interpreted here as a fossil stress configuration no longer kinematically compatible with the present stress field. The absence of first-order stress reorganization during eastward migration of the extensional front supports persistence of this regional stress architecture over ~3.5 Ma.

The main results can be summarized as follows:

1. The dominant Late Pliocene–Quaternary tensional stress field is consistently Andersonian across the IEP. Independent stabilization of stress tensors from Structural Sites to Fault Groups and Fault Supergroups, together with the systematic increase of the Andersonian Index with spatial aggregation, demonstrates that the vertical–horizontal stress geometry is a robust regional property rather than a methodological artifact. Stress ratio (ϕ) displays a modest southward increase associated with relative amplification of σ_2, whereas differential stress ($\sigma_1 - \sigma_3$) is persistently high, indicating elevated deviatoric conditions across the IEP.

2. The present configuration of the IEP reflects an advanced stage of a migrating extensional regime. After an early, spatially restricted transtensional phase, deformation evolved into mature Andersonian extension governed primarily by lithostatic gradients and gravitational potential energy contrasts, while maintaining first-order geometric coherence during outward migration of deformation bands.
3. The stress field exhibits an arcuate organization expressed across multiple spatial wavelengths. The double-arc geometry of the IEP is best interpreted as a primary crustal feature developed in spatial coherence with regional Moho curvature and crustal-thickness gradients. The continuity of σhmin trajectories and the absence of discrete regional rotation domains argue against progressive secondary oroclinal bending and instead support inheritance from deep-seated lithospheric structure.
4. Progressive aggregation from Structural Sites to Fault Groups and Fault Supergroups demonstrates that spatial upscaling filters short-wavelength perturbations while preserving the first-order regional stress geometry. This hierarchical stabilization highlights the mechanical coherence of the IEP from outcrop to crustal scale and provides a reproducible framework for stress-field reconstruction in complex extensional provinces.
5. Strong agreement among geological, seismological, and geodetic stress indicators enables the construction of a hybrid map of tensional/extensional axes through time. Quantified angular discrepancies constrain the scale of local stress rotations and define objective limits of dataset resolution, reinforcing the reliability of the reconstructed regional stress architecture.
6. The PILOT database constitutes one of the most extensive geological stress-tensor datasets currently available for an actively deforming intraplate region. It demonstrates that geological stress inversion can yield mechanically meaningful constraints on persistent deformation where stress regimes remain stable over geological timescales, and that its integration into global stress compilations would substantially enhance interpretation of long-lived extensional systems.

Some limitations remain. Geological stress inversion depends on data density, exposure quality, and rigorous discrimination of multi-phase slip histories. While stress orientations are robustly constrained, relative stress magnitudes and ellipsoid shapes require further investigation, particularly along the outer extensional front where structural exposure is reduced. Nevertheless, in slowly deforming and low-strain regions such as the IEP, geological datasets provide temporal depth inaccessible to short-term geophysical observations alone. The time-integrated reconstruction presented here establishes a mechanically coherent regional stress framework within a still-active seismotectonic province. Its internal consistency supports applications in three-dimensional fault segmentation, seismic hazard assessment, and geodynamic modelling. More broadly, the methodological approach developed here is transferable to other intraplate or persistently deforming regions, offering a strategy to reconcile geological inheritance with present-day tectonic processes.

METHODS

Structural framework, boundaries, and temporal evolution of the IEP

Fault traces of the Intra-Apennine Extensional Province (IEP), derived from the QUIN 1.0 and QUIN 2.0 fault databases[8,9], were systematically expanded to incorporate additional peripheral faults extending beyond the previously mapped fault alignments, mainly toward the east and west, while remaining structurally coherent with the main extensional belt (Fig.1a; Supplementary Fig.1a). These additional traces, highlighted in yellow in Supplementary Figure 1, were compiled from the Geological map of Italy (scale 1:100.000 and 1:50.000; https://www.isprambiente.gov.it/it/attivita/suolo-e-territorio/cartografia/carte-geologiche-e-geotematiche), the ITHACA database[11], and targeted field surveys conducted at higher detail. Regional-scale geological maps were additionally considered to constrain the broader tectonic framework and fault architecture[12,13,14,15,16]. Regional fault compilations, including the Active Faults of Eurasia Database (AFEAD)[97], were also consulted.

All figures were generated within a single GIS project referenced to WGS84 (GCS_WGS_1984) and projected in a Lambert Conformal Conic coordinate system (central meridian 13°E; standard parallels 39° and 45°; latitude of origin 42°; units in meters). Maps and graphical representations were originally produced by the authors using ArcGIS Pro (v. 3.6.4; Esri; https://www.esri.com/en-us/arcgis/products/arcgis-pro/overview), CorelDRAW Graphics Suite (Corel Corporation; v. 2020; https://www.coreldraw.com), and MOVE (Petroleum Experts Ltd.; v. 2019.1; https://www.petex.com/products/move-suite/). No copyrighted maps or previously published figures were reused or modified.

The compiled fault pattern was hierarchically organized to define the multi-scale Fault Striation Pair (FSP) aggregation domains used for the PILOT stress inversion, together with the structural boundaries and internal zoning of the IEP (Figs.1,2). Four schematic structural levels were distinguished:

1. Fault segments, articulated in fault sections, generally extending for ~10–25 km, hosting the Structural Sites (SS; PILOT Datasets 1a and 1b[17]) and mainly corresponding to QUIN host faults[8,9] and their integrations (Fig.1a). These structures commonly consist of individual fault traces displaying local along-strike overlaps (step-overs) or gaps, together with minor perpendicular-to-strike separations generally <1 km.
2. Master faults, generally extending for ~25–50 km, used to define the polygonal domains of the Fault Groups (Fig.5). They commonly consist of multiple connected fault segments displaying step-overs or gaps and perpendicular-to-strike separations generally on the order of 1–2 km.
3. Neighboring master-fault alignments (fault traces A–V and a–q in Fig.2), generally extending for ~100 ± 30 km and commonly consisting of two to three master faults connected through step-overs or gaps generally <3–5 km, locally associated with significant bending zones and perpendicular-to-strike separations on the order of 2–3 km, while maintaining coherent dip polarity and similar kinematic behaviour.
4. Regional master-fault alignments (such as a, b, and y in Fig.2), each extending up to ~350–400 km and commonly consisting of multiple neighboring master faults characterized by along-strike overlaps or gaps reaching several kilometres and average perpendicular-to-strike separations of at least ~5 km, while maintaining coherent dip polarity, compatible kinematic behaviour, comparable deformation-axis patterns, and similar timing of fault initiation.

Fault traces hosting the Early-Stage FSP population structures (black traces in Fig.1b) were treated separately and derived from available literature[18,19,20,23,24]. They mostly consist of approximately E-W south-dipping fault with left-lateral transtensional kinematics.

To investigate the spatio-temporal distribution of extensional structures within the IEP, characterized by progressive eastward rejuvenation of fault activity[43], fault-initiation ages compiled in the QUIN host-fault datasets[8,9] were analysed together with additional literature constraints[14,30,39,40,41,42]. The analysed data are spatially discontinuous and derived from heterogeneous stratigraphic and geomorphic markers that are not always temporally equivalent; therefore, they cannot be treated as discrete, directly comparable time markers. To address this limitation, IEP fault sectors sharing comparable plausible ranges of fault-initiation ages were identified in map view, accounting for the uncertainty and variability of the available chronological constraints. The resulting scheme highlights broad longitudinal sectors with partially overlapping initiation-age ranges. Individual initiation estimates may locally vary by up to ~1 Ma, reflecting diachroneity, stratigraphic uncertainty, geomorphic variability, and inconsistencies among published interpretations. In Figure 1b, the coloured bars represent plausible initiation-age ranges for each longitudinal alignment rather than total durations of fault activity, whereas dashed lines indicate the possible temporal interval for persistence of activity.

The PILOT stress database

The PILOT Stress Database[17] is primarily based on the multi-scale inversion of 8,206 fault–striation pairs (FSP) measured along or near Late Pliocene–Quaternary fault traces within the IEP. The FSP input data derives mainly from QUIN 1.0 and 2.0[8,9], supplemented by an additional ~8% of data compiled from literature. All bibliographic references are documented in the README file accompanying the Zenodo release of the database[17].

The database is organized into four distinct dataset types, provided as four separate Excel files:

- Dataset 1 – Structural Site (SS) kinematic PBT stress inversion, subdivided into 1a with θ=30° and 1b with θ=45°;
- Dataset 2 – Fault Group (FG) full-tensor stress inversion, subdivided into 2a (prevailing) and 2b (subsidiary);
- Dataset 3 – Fault Supergroup (FSG) full-tensor stress inversion;
- Dataset 4 – Multi-Source tensional axes (T-hybrid map).

Dataset 1 consists of stress parameters calculated for 841 SS using the kinematic PBT stress inversion method[45]. SS may include data from single or nearby outcrops (up to 5 km apart) that are geometrically and kinematically coherent (Supplementary Fig.2). In ~40% of the cases, individual SS were grouped into Composite SS in order to increase the number of available FSPs and improve the statistical robustness of the inversion (Fig S3a-b). To preserve spatial completeness and capture local stress deviations, PILOT Dataset 1 also includes SS with fewer than six FSP, particularly along poorly exposed or difficult-to-access fault segments. These sites document local slip geometries; they were inverted for completeness but were excluded from formal quality ranking attribution (Supplementary Tab.2a). Approximately 78% of SS are located on-fault (within 500 m of the host-fault trace), ~10% off-fault (within 500 m in hanging-wall basin deposits), ~4% are associated with antithetic faults, and ~8% correspond to transverse structures (angle >45° relative to the host fault).

Datasets 2 and 3 include stress parameters obtained by grouping the FSP data into 89 Fault Groups and 9 Fault Supergroups, respectively, and performing formal full-tensor stress inversion using the MSATSI code[46]. Datasets 2a and 3 refer to the inversion of the prevailing kinematic populations, whereas Dataset 2b corresponds to the associated residual populations.

Dataset 4 provides a spatially continuous and time-integrated representation of extensional deformation in the IEP. Tensional and extensional trends, resampled onto a 10×10 km grid, are derived from three independent data sources: geological Shmin from PILOT Dataset 1a, seismological T-axes from published focal-mechanism catalogues[36,37], and geodetic εhmax from the strain-rate field computed in this study using GNSS velocities[52]. For each grid cell, Dataset 4 provides the circular mean trend of the available directional data, referred to as the T-hybrid axis, together with the corresponding angular spread.

Acronyms and stress-tensor notation used throughout the manuscript are summarized in Supplementary Tab.1a. Abbreviations identifying the major fault systems referenced in the main text are shown in Supplementary Fig.1a.

Stress inversion multi-step workflow

Given the different sizes of the FSP populations at the three hierarchical levels, SS (~10 FSP on average), FG (~100 FSP), and FSG (~900 FSP), we applied different inversion strategies appropriate to dataset size and statistical robustness: a statistical PBT inversion for SS (local scale) and a full-tensor inversion for FG and FSG (regional to crustal scale). All inversions were implemented through a dedicated MATLAB workflow developed for this study. The pipeline integrates pre- and post-processing scripts with established inversion routines[45,46] and follows a progressive filtering and tensor-optimization logic inspired by Win-TENSOR[90]. The procedure is organized into three sequential steps.

Step 1 - Automated kinematic pre-filtering

For each SS, FG and FSG, the principal deformation axes (P,B,T) of the included FSP were first computed using a kinematic approach based on the Mohr–Coulomb fracture criterion[45] with a reference fracture angle θ=30°, consistent with Andersonian brittle mechanics in the upper crust[63]. The angular deviation between the computed PBT-axes and the PBT orientation of each FSP was calculated. FSP with a PBT deviation lower than the mean plus one standard deviation were classified as kinematically compatible and defined as the prevailing population. The remaining FSP were classified as residual. Residual FSP were either excluded from subsequent stress inversion or inverted separately (Dataset 2b) to evaluate secondary or local stress components. This automated filtering ensures internal kinematic coherence before tensor estimation and formalizes procedures often applied manually.

Step 2 - Stress-inversion

For SS datasets, a statistical PBT inversion[49,62] was applied to the kinematically compatible FSP. The inversion is based on a 3×3 matrix constructed from the direction cosines of the P and T axes and provides estimates of principal stress orientations (S1-S2-S3) and their angular dispersion. The workflow includes spherical-to-Cartesian transformations. The fracture angle θ, defined as the angle between the fault plane and the compressional axis (P), is required only for the kinematic PBT inversion and associated conjugate-plane reconstruction at SS scale, whereas the full-tensor inversion applied to FG and FSG datasets does not require a prescribed fracture angle, as stress orientation and relative magnitudes are solved directly from slip-vector misfit minimization.

Because θ cannot be directly constrained from fault-slip data, different mechanically plausible values were tested (Supplementary Fig.4). In addition to the two classical reference configurations commonly adopted in fault-slip analysis[62,63] and used in QUIN datasets (θ=30° and θ=45°)[8,9], an intermediate value of θ=36°[98] was also evaluated. Comparison of the resulting stress-axis distributions shows that decreasing θ progressively tightens the clustering of S1 toward near-vertical plunges and of S3 toward near-horizontal orientations. Among the tested configurations, θ=30° produces the closest approximation to an Andersonian vertical–horizontal stress configuration.

For FG and FSG datasets, a full-tensor inversion was performed using the SATSI method implemented through the MSATSI MATLAB package[46]. This method minimizes the misfit angle (α) between observed slip vectors and resolved shear stress, solving simultaneously for stress orientation and relative magnitudes.

For each tensor, the inversion provides:

1. Orientation (trend/plunge) of σ_1, σ_2, and σ_3, with associated standard deviations.
2. Principal stress eigenvalues (compression-positive convention; $\sigma_1 \geq \sigma_2 \geq \sigma_3$).
3. Stress ratio $\phi=(\sigma2-\sigma3)/(\sigma1-\sigma3)$[49], with standard deviation.
4. Normalized differential stress, $d=(\sigma1-\sigma3)/\max(\sigma1-\sigma3)$, ranging from 0 to 1 and scaled to the maximum $(\sigma1-\sigma3)$ value within the dataset (after[50]).

Results were iteratively refined to maximize internal consistency. Bootstrap resampling (n=2000) was applied to estimate 95% confidence intervals for stress-axis orientations, stress ratio (ϕ), and derived horizontal stress directions (Fig.6). Mechanical layering and alternative subsurface fault geometries are not explicitly parameterized within the inversion workflow and therefore are not independently propagated into the stress-tensor solution.

Step 3- Post-inversion processing

Post-processing included the following developments.

a. Maximum and minimum horizontal stresses computation following[47]. The correction produces an average angular difference of ~10° between Shmin/Shmax and the corresponding principal stress axes.

b. Conjugate failure planes and associated slip vectors were computed by solving the inverse problem under the Mohr–Coulomb failure criterion, based on the resolved shear stress acting on optimally oriented planes. For SS tensors, conjugate planes were calculated assuming θ=30° (PILOT Dataset 1a) and θ=45° (PILOT Dataset 1b); among the two predicted planes, the one minimizing the angular misfit (a) between observed slip vectors and the direction of resolved shear stress was retained. For FG and FSG tensors (PILOT Datasets 2a, 2b, and 3), θ=45° was adopted and both conjugate failure planes were preserved.
c. Separate ranking schemes were defined for SS and FG/FSG datasets. For SS (PBT inversion), quality criteria were adapted from established PBT-based schemes[90] and include FSP number, ratio of inverted FSP, data quality index (QI), mean PBT deviation, and its standard deviation (Supplementary Tab.2a). SS with fewer than 6 FSP were a priori excluded from the quality ranking attribution. For FG and FSG (full-tensor inversion), the Quality Ranking (QR) criteria were adapted from Lundstern & Zoback[4] (Supplementary Tab.2b). Ranking incorporates bootstrap-derived dispersion of σ1, σ2, σ3, and ϕ as quantitative measures of tensor stability. Only FG with ≥15 FSP and an inverted/total FSP ratio ≥0.75 were retained. Multimodal bootstrap solutions (e.g., σ1–σ2 or σ2–σ3 interchangeability) automatically result in class D assignment. Quality classes range from A (Excellent) to D (Poor).
d. SS tensors were kinematically classified using rake-based bins (~15° intervals of slip-vector rake), following standard fault-slip classification criteria[99], whereas FG and FSG tensors were classified using the plunge-based equiangular triangular diagram of Kagan[48], here discretized into 15° bins (Supplementary Tab.3).
e. For FG and FSG (full tensor inversion), the Lundstern & Zoback[4] correction was applied to derive the orientations of σhmax and σhmin from the inverted principal stress tensor (Supplementary Fig.6).
f. To jointly visualise stress ratio ($\phi=(\sigma_2-\sigma_3)/(\sigma_1-\sigma_3)$) and normalized differential stress ($d=(\sigma1-\sigma3)/\max(\sigma1-\sigma3)$), we implemented a Python tool reproducing the triangular diagram of Ramsay & Lisle[50] (Fig.7b). In this representation, differences between stress eigenvalues ($\sigma_1-\sigma_2$, $\sigma_2-\sigma_3$) are plotted on Cartesian axes; constant-ϕ states align along rays from the origin, while distance from the origin reflects normalized differential stress. Ellipsoid shape classification is based on the stress ratio φ and subdivided into eight bins (Δφ=0.125) as follows:
    - strongly prolate (0≤φ<0.125)
    - prolate (0.125≤φ<0.250)
    - weakly prolate (0.250≤φ<0.375)
    - near-triaxial (prolate side) (0.375≤φ<0.500)
    - near-triaxial (oblate side) (0.500≤φ< 0.625)
    - weakly oblate (0.625≤φ<0.750)
    - oblate (0.750≤φ<0.875)
    - strongly oblate (0.875 ≤ φ < 1.000)

   Intervals are left-closed and right-open, with φ constrained to the range 0 ≤ φ < 1.
g. Andersonian Index (AI): definition and implementation. To quantify the degree to which a stress tensor approaches Andersonian dip-slip and strike-slip end-member configurations, we introduce the Andersonian Index (AI) (Supplementary Tab.7). AI measures stress-tensor obliquity based on the plunge (in degrees) of the intermediate principal stress axis (δB), constrained to the interval 0°–90°. AI reaches its minimum value (AI=0) when δB=45°, corresponding to maximum geometric departure from Andersonian configurations, and increases symmetrically toward δB=0° (dip-slip) and δB=90° (strike-slip), where AI=10. Because Andersonian end members are defined by one principal stress axis being vertical and the other two horizontal, the plunge of σ_2 provides a direct geometric measure of deviation from these configurations. AI therefore quantifies geometric proximity to Andersonian end members but does not, by itself, determine the kinematic regime.

AI is defined on a continuous 0–10 scale:

$AI=10\times|1-2\delta B/90|$ with δB constrained to [0°,90°].

For descriptive purposes, AI values are grouped into three classes: A=AI>6.7; B=3.3≤AI≤6.7; C=AI<3.3.

Stress Mapping and Geospatial Integration

PILOT stress maps and analytical products

Stress-map views include horizontal stress orientations, interpolated Shmin trajectories, and pseudo-focal mechanisms providing an intuitive representation of tensor kinematics (Figs.3-5,8 and Supplementary Figs.2,5,6). All thematic maps were produced within the same GIS framework described above for the fault architecture. Additional products, within the same figures, include rose diagrams, bootstrap stereoplots, stereonets, triangular projections of principal stress axes, and a triangular diagram representing stress ratio and normalized differential stress (Fig.7). A complete stereographic atlas for FG inversions is provided in Supplementary Table 9.

FG stress ratio values and SS-derived Shmin trends were projected orthogonally onto a non-linear longitudinal transect crossing the IEP (~1000 km; trace in Fig.3b) to visualise along-strike stress variability.

Moho depth surface

The Moho surface (Fig.8) was reconstructed within the same GIS framework, enabling direct comparison with the stress field results. We integrated legacy depth contour maps based on seismological profiles[56,57,58], the EP CRUST model updated to 2024[55], and receiver-function datasets[42,100]. These inputs were homogenized and interpolated into isocontour depth lines, then converted into a 3D surface using MOVE software (Petex, 2021). The resulting Moho surface provides a lithospheric framework for integration with geological structures and stress-field data.

Geodetic strain rate map

The horizontal dilatation strain-rate field shown in Fig.9, together with the directions and magnitudes of the principal horizontal strain-rate axes, was recomputed in this study from the GNSS velocity dataset of[52]. Strain rates were calculated using VISR software[61], following a workflow consistent with Sparacino et al.[101], to obtain a strain-rate field fully aligned with the PILOT framework in terms of spatial resolution, map projection, and sampling strategy. Only GNSS stations with ≥5 years of continuous observations were retained to minimize seasonal and post-seismic effects. Velocity interpolation used optimal weighting parameters[38], based on sensitivity tests tailored to the Italian GNSS network. The maximum horizontal extensional strain axes (εhmax) were extracted as principal eigenvectors of the horizontal strain-rate tensor and initially mapped on a 0.01°×0.01° grid. These data were then resampled onto a regular 10×10 km grid using the Find Nearest Feature tool in QGIS (maximum distance: 200 m). Directions of both contractional (εhmin) and extensional (εhmax) axes were obtained from VISR shear-strain outputs using a dedicated Python script. Spatial resolution varies with GNSS station density (Supplementary Fig.8b). Central Italy is characterized by higher resolution, whereas data-sparse regions, such as Northern Calabria, display lower resolving power. Along the IEP, the horizontal geodetic strain-rate field is resolved at an average spatial scale of ~13 km. Consistently, wavelet-based analyses[102] indicate that VISR spatial scale parameters q=8–10 correspond to characteristic wavelengths of ~7–27 km.

Hybrid T-axis map

The T-hybrid axis map (Fig.9a), providing a high-resolution, time-integrated picture of tension/extension across the IEP, was built within the same GIS framework to ensure direct comparability with structural layers (Figs.1,2) and with geodetic and seismological layers (Supplementary Figs. 7 and 8). PILOT Dataset 4[17] compiles tensional and extensional trends from three independent sources (geology, seismology, geodesy), all projected onto a common 10×10 km grid. This resolution optimizes data density and directional homogeneity.

Input data include:

(i) Shmin from SS in PILOT Dataset 1a (quality ranks A–C only; Early Stage and transverse SS excluded);
(ii) εhmax derived from the GNSS velocity field (Fig.9; Supplementary Fig.8);
(iii) T-axes from focal mechanisms, extracted from the RCMT catalogue[36] (1908–2014; Mw3.9–7.0) and the INGV TDMT database[37] (2015–2023; Mw3.0–6.5) (Supplementary Fig.7a). A total of 433 extensional events (Supplementary Fig.7b) with focal depths≤16 km were retained, in agreement with recent estimates of Apennine seismogenic thickness[38], derived from the CLASS relocated seismicity catalogue[35].

Stress2Grid[59] was used to structure the grid and integrate the datasets. The computation of T-hybrid axes was performed in two steps: first, by calculating circular averages of T-axes within each grid cell for each available dataset separately, and then by combining these dataset-specific averages through circular averaging to obtain a single T-hybrid axis for each grid cell. The angular spread (Δ) was defined as half of the acute angle (0°–45°) between the two most divergent azimuthal trends among contributing datasets. This definition provides a conservative measure of directional divergence centered on the hybrid axis.
Based on Δ and the number of contributing data types, the following quality classes were assigned:

- A+: Δ ≤ 10° with 3 data types;
- A: Δ ≤ 10° with 2 data types;
- B: 10°<Δ ≤ 20° with 2 or 3 data types;
- C: 20°<Δ ≤ 30° with 2 or 3 data types;
- D: 30°<Δ ≤ 45° with 2 or 3 data types.

A map-view representation of T-hybrid axes and angular spreads is provided in Fig.9.
The resulting grid-point dataset constitutes PILOT Dataset 4 and forms the basis both for the T-hybrid map (Fig.9a) and for the FSG-scale directional synthesis reported in Supplementary Table 10.

DATA AVAILABILITY

The PILOT Stress Database (Andrenacci et al.[17]) is publicly available through the Zenodo repository (https://zenodo.org/records/18836369). The release includes four Excel files corresponding to Datasets 1–4. A detailed README file accompanies the database and documents its structure, attribute definitions, and the bibliographic sources used for compilation. Additional figures, tables, and derived products supporting the findings of this study are provided in the Supplementary Information.

Input fault/striation pairs for the PILOT stress inversion and corresponding PBT-axes are available from the Pangaea (https://doi.pangaea.de/10.1594/PANGAEA.934802) and Zenodo (https://doi.org/10.5281/zenodo.8414734) repositories, for the 1.0 and 2.0 releases, respectively.

Geological base maps and fault traces consulted in this study are available through the ISPRA Geological Cartography Portal at https://www.isprambiente.gov.it/it/attivita/suolo-e-territorio/cartografia/carte-geologiche-e-geotematiche; the QUIN 1.0 Host Fault Database for Central Italy (Lavecchia et al.[9]), available on Zenodo (https://doi.org/10.5281/zenodo.5603004). QUIN 2.0 Host Fault Database for Southern Italy (Lavecchia et al.[8]), available on Zenodo repository (https://doi.org/10.5281/zenodo.8414480). The Italian active fault ITHACA database[11] (available at https://sgi.isprambiente.it/ithaca/viewer/index.html). Active Faults of Eurasia Database (AFEAD)[97] at http://neotec.ginras.ru/index/english/database_eng.html

ACKNOWLEDGEMENTS

This work was initially developed within the framework of the PRIN 2017 MUSE 4D project, coordinated by G.L., and was subsequently further developed within the DEFENS Project, coordinated by S.B. We thank Michele Carafa for carefully reading the pre-submission version of the manuscript and for his useful comments and discussions. We also sincerely thank the Editor and the anonymous reviewers for their constructive and insightful comments, which significantly improved the clarity and robustness of the manuscript. We thank Daniele Cirillo for his valuable support in the reconstruction of the Moho surface.

AUTHOR CONTRIBUTIONS

G.L. and C.A. contributed equally to this paper. Conceptualisation: G.L., C.A.; Investigation: G.L., C.A., F.P., S.B.; Methodology: G.L., C.A., F.P.; Data curation and analysis: G.L., C.A., F.P., S.B.; Funding acquisition: S.B.; Supervision: G.L., F.B., R.d.N.; Writing-original draft: G.L., C.A., S.B.; Writing-review and editing: G.L., C.A., S.B., F.P., F.B., R.d.N.

FUNDING

The research was supported by the Ministry of University and Research of Italy with the funding of the DEFENS Project (Bando FIS2 - D.D. 1236-01/08/2023) to the project P.I. Bello Simone. Proj. code: FIS-2023-00179; CUP: D53C24005460001.

REFERENCES

1. Zoback ML*, et al.* Global patterns of tectonic stress. *Nature* **341**, 291-298 (1989).
2. Heidbach O*, et al.* The World Stress Map database release 2016: Crustal stress pattern across scales. *Tectonophysics* **744**, 484-498 (2018).
3. Levandowski W, Herrmann RB, Briggs R, Boyd O, Gold R. An updated stress map of the continental United States reveals heterogeneous intraplate stress. *Nature Geoscience* **11**, 433-437 (2018).
4. Lundstern JE, Zoback MD. Multiscale variations of the crustal stress field throughout North America. *Nat Commun* **11**, 1951 (2020).
5. Martínez-Garzón P, Heidbach O, Bohnhoff M. Contemporary stress and strain field in the Mediterranean from stress inversion of focal mechanisms and GPS data. *Tectonophysics* **774**, (2020).
6. Mariucci MT, Montone P. Database of Italian present-day stress indicators, IPSI 1.4. *Sci Data* **7**, 298 (2020).
7. Reiter K, Heidbach O, Ziegler MO. Impact of faults on the remote stress state. *Solid Earth* **15**, 305-327 (2024).
8. Lavecchia G*, et al.* QUIN 2.0 - new release of the QUaternary fault strain INdicators database from the Southern Apennines of Italy. *Sci Data* **11**, 189 (2024).
9. Lavecchia G*, et al.* QUaternary fault strain INdicators database - QUIN 1.0 - first release from the Apennines of central Italy. *Sci Data* **9**, 204 (2022).
10. Rovida A, Locati M, Camassi R, Lolli B, Gasperini P. The Italian earthquake catalogue CPTI15. *Bulletin of Earthquake Engineering* **18**, 2953-2984 (2020).
11. ITHACA WG. ITHACA (ITaly HAzard from CApable faulting), A database of active capable faults of the Italian territory. Version December 2019. (ed Italy IGSo) (2019).
12. Bigi G*, et al. Structural Model of Italy scale 1:500.000 (Sheets 1-6)*. SELCA (1990-1992).
13. Bonardi G*, et al.* Carta geologica dell'Appennino meridionale 1:250.000. (eds BONARDI G, D'ARGENIO B, PERRONE V) (1988).
14. Molli G*, et al.* Active Fault Systems in the Inner Northwest Apennines, Italy: A Reappraisal One Century after the 1920 Mw ~6.5 Fivizzano Earthquake. *Geosciences* **11**, (2021).
15. Vezzani L, Festa A, Ghisetti FC, Vezzani L, Festa A, Ghisetti FC. Geology and Tectonic Evolution of the Central-Southern Apennines, Italy. In: *Geology and Tectonic Evolution of the Central-Southern Apennines, Italy*). Geological Society of America (2010).

16. Martelli L*, et al.* Seismic hazard of the Northern Apennines based on 3D seismic sources. *Journal of Seismology* **21**, 1251-1275 (2017).
17. Andrenacci C, Bello S, Pietrolungo F, Brozzetti F, de Nardis R, Lavecchia G. PILOT Extensional Stress Database v1.0.). 1.0 edn (2026).
18. Tansi C, Muto F, Critelli S, Iovine G. Neogene-Quaternary strike-slip tectonics in the central Calabrian Arc (southern Italy). *J Geodyn* **43**, 393-414 (2007).
19. Pace B, Boncio P, Lavecchia G. The 1984 Abruzzo earthquake (Italy): An example of seismogenic process controlled by interaction between differently oriented synkinematic faults. *Tectonophysics* **350**, 237-254 (2002).
20. Brozzetti F*, et al.* Newly identified active faults in the Pollino seismic gap, southern Italy, and their seismotectonic significance. *J Struct Geol* **94**, 13-31 (2017).
21. Boncio P, Dichiarante AM, Auciello E, Saroli M, Stoppa F. Normal faulting along the western side of the Matese Mountains: Implications for active tectonics in the Central Apennines (Italy). *Journal of Structural Geology* **82**, 16-36 (2016).
22. Bertotti G, Capozzi R, Picotti V. Extension controls Quaternary tectonics, geomorphology and sedimentation of the N-Appennies foothills and adjacent Po Plain (Italy). *Tectonophysics* **282**, 291-301 (1997).
23. Boncio P, Brozzetti F, Lavecchia G. State of stress in the Northern Umbria-Marche Apennines (Central Italy): inferences from microearthquake and fault kinematic analyses. In: *Annales Tectonicae*) (1996).
24. Tavani S*, et al.* Segmentation of the Apenninic Margin of the Tyrrhenian Back-Arc Basin Forced by the Subduction of an Inherited Transform System. *Tectonics* **40**, (2021).
25. Battistelli M*, et al.* Bridging the Gap Between Active Faulting and Deformation Across Normal-Fault Systems in the Central–Southern Apennines (Italy): Multi-Scale and Multi-Source Data Analysis. *Remote Sensing* **17**, (2025).
26. Brozzetti F, Boncio P, Lavecchia G, Pace B. Present activity and seismogenic potential of a low-angle normal fault system (Città di Castello, Italy): Constraints from surface geology, seismic reflection data and seismicity. *Tectonophysics* **463**, 31-46 (2009).
27. Lavecchia G, Brozzetti F, Bello S, de Nardis R. Mapping fault architecture from depth to surface: integrating microseismicity and structural geology in low-strain Apennine regions. *Journal of Structural Geology* **200**, (2025).
28. Brozzetti F. The Campania-Lucania Extensional Fault System, southern Italy: A suggestion for a uniform model of active extension in the Italian Apennines. *Tectonics* **30**, 1-26 (2011).
29. Andrenacci C*, et al.* Reappraisal and Analysis of Macroseismic Data for Seismotectonic Purposes: The Strong Earthquakes of Southern Calabria, Italy. *Geosciences* **13**, (2023).
30. Lavecchia G. The Tyrrhenian-Apennines system: structural setting and seismotectogenesis. *Tectonophysics* **147**, 263-296 (1988).
31. Doglioni C. A proposal of kinematic modelling for W-dipping subductions - possible applications to the Tyrrhenian-Apennines system. *Terra Nova* **3**, 423-434 (1991).
32. Faccenna C, Becker TW. Topographic expressions of mantle dynamics in the Mediterranean. *Earth-Science Reviews* **209**, 103327 (2020).
33. Trippetta F*, et al.* From mapped faults to fault-length earthquake magnitude (FLEM): a test on Italy with methodological implications. *Solid Earth* **10**, 1555-1579 (2019).

34. Lavecchia G, de Nardis R, Ferrarini F, Cirillo D, Bello S, Brozzetti F. Regional seismotectonic zonation of hydrocarbon fields in active thrust belts: a case study from Italy. In: *Building Knowledge for Geohazard Assessment and Management in the Caucasus and other Orogenic Regions* (eds Bonali F. L., Mariotto F. P., Tsereteli N.). Springer Netherlands (2021).
35. Latorre D, Di Stefano R, Castello B, Michele M, Chiaraluce L. An updated view of the Italian seismicity from probabilistic location in 3D velocity models: The 1981–2018 Italian catalog of absolute earthquake locations (CLASS). *Tectonophysics* **846**, (2023).
36. Pondrelli S, Visini F, Rovida A, D'Amico V, Pace B, Meletti C. Style of faulting of expected earthquakes in Italy as an input for seismic hazard modeling. *Natural Hazards and Earth System Sciences* **20**, 3577-3592 (2020).
37. Scognamiglio L, Tinti E, Quintiliani M. Time Domain Moment Tensor [Data Set]. (ed (INGV) INdGeV) (2006).
38. Nucci R, Serpelloni E, Faenza L, Garcia A, Belardinelli ME. Geodetic Strain Rates and Seismicity Rates Along the Apennines (Italy). *Journal of Geophysical Research: Solid Earth* **130**, (2025).
39. Cavinato GP, Celles PGD. Extensional basins in the tectonically bimodal central Apennines fold-thrust belt, Italy: Response to corner flow above a subducting slab in retrograde motion. *Geology* **27**, 955-958 (1999).
40. Barchi MR. The Neogene-Quaternary evolution of the Northern Apennines: crustal structure, style of deformation and seismicity. *J Virtual Explor* **36**, (2010).
41. Cosentino D, Cipollari P, Marsili P, Scrocca D. Geology of the central Apennines: a regional review. *Journal of the Virtual Explorer* **36**, (2010).
42. Lanari R, Reitano R, Faccenna C, Piana Agostinetti N, Ballato P. Surface and Crustal Response to Deep Subduction Dynamics: Insights From the Apennines, Italy. *Tectonics* **42**, (2023).
43. Basili R, Barba S. Migration and shortening rates in the northern Apennines, Italy: implications for seismic hazard. *Terra Nova* **19**, 462-468 (2007).
44. Fubelli G, Gori S, Falcucci E, Galadini F, Messina P. Geomorphic signatures of recent normal fault activity versus geological evidence of inactivity: Case studies from the central Apennines (Italy). *Tectonophysics* **476**, 252-268 (2009).
45. Marrett R, Allmendinger RW. Kinematic analysis of fault-slip data. *Journal of Structural Geology* **12**, 973-986 (1990).
46. Martinez-Garzon P, Kwiatek G, Ickrath M, Bohnhoff M. MSATSI: A MATLAB Package for Stress Inversion Combining Solid Classic Methodology, a New Simplified User-Handling, and a Visualization Tool. *Seismological Research Letters* **85**, 896-904 (2014).
47. Lund B, Townend J. Calculating horizontal stress orientations with full or partial knowledge of the tectonic stress tensor. *Geophysical Journal International* **170**, 1328-1335 (2007).
48. Kagan YY. Double-couple earthquake focal mechanism: random rotation and display. *Geophysical Journal International* **163**, 1065-1072 (2005).
49. Angelier J. Determination of the mean principal directions of stresses for a given fault population. *Tectonophysics* **56**, 17-26 (1979).
50. Ramsay JG, Lisle RJ. *The techniques of modern structural geology, volume 3: Applications of continuum mechanics in structural geology* (2000).

51. Lisle RJ, Orife TO, Arlegui L, Liesa C, Srivastava DC. Favoured states of palaeostress in the Earth's crust: evidence from fault-slip data. *Journal of Structural Geology* **28**, 1051-1066 (2006).
52. Serpelloni E*, et al.* Surface Velocities and Strain-Rates in the Euro-Mediterranean Region From Massive GPS Data Processing. *Frontiers in Earth Science* **10**, (2022).
53. D'Agostino N. Complete seismic release of tectonic strain and earthquake recurrence in the Apennines (Italy). *Geophysical Research Letters* **41**, 1155-1162 (2014).
54. Lacombe O. Do fault slip data inversions actually yield “paleostresses” that can be compared with contemporary stresses? A critical discussion. *Comptes Rendus Géoscience* **344**, 159-173 (2012).
55. Molinari I, Morelli A. EPcrust: a reference crustal model for the European Plate. *Geophysical Journal International* **185**, 352-364 (2011).
56. R. Nicolich R, Laigle M, Hirn A, Cernobori L, Gallart J. Crustal structure of the Ionian margin of Sicily: Etna volcano in the frame of regional evolution. *Tectonophysics* **329**, 121-139 (2000).
57. Locardi E, Nicolich R. Geodinamica del Tirreno e dell'Appennino centro-meridionale: la nuova carta della Moho. *Mem Soc Geol It* **41**, 121-140 (1988).
58. Cassinis R, Scarascia S, Lozej A. The deep crustal structure of Italy and surrounding areas from seismic refraction data. A new synthesis. *Bollettino della Societa Geologica Italiana* **122**, 365-376 (2003).
59. Ziegler M, Heidbach O. Matlab script Stress2Grid v1.1.). GFZ Data Services (2019).
60. Chiodini G*, et al.* Carbon dioxide Earth degassing and seismogenesis in central and southern Italy. *Geophysical Research Letters* **31**, (2004).
61. Shen ZK, Wang M, Zeng Y, Wang F. Optimal Interpolation of Spatially Discretized Geodetic Data. *Bulletin of the Seismological Society of America* **105**, 2117-2127 (2015).
62. Sperner B, Ratschbacher L, Rolf O. Fault-striae analysis: a Turbo Pascal package for graphical presentation and reduced stress tensor calculation. *Computers & Geosciences* **19**, 1361-1388 (1993).
63. Célérier B. Seeking Aderson's faulting in seismicity: A centennial celebration. *Reviews of Geophysics* **46**, 1-34 (2008).
64. Della Vedova B., Bellani S., P. PGS. Deep temperatures and surface heat flow distribution. In: *Anatomy of an Orogen: the Apennines and Adjacent Mediterranean basin.* (eds G. B. Vai, Martini IP). Kluwer Academic Publishers (2001).
65. Ring U, Glodny J, Will T, Thomson S. The Hellenic Subduction System: High-Pressure Metamorphism, Exhumation, Normal Faulting, and Large-Scale Extension. *Annual Review of Earth and Planetary Sciences* **38**, 45-76 (2010).
66. Platt JP, Behr WM, Johanesen K, Williams JR. The Betic-Rif Arc and Its Orogenic Hinterland: A Review. *Annual Review of Earth and Planetary Sciences* **41**, 313-357 (2013).
67. Sonder LJ, Jones CH. Western United States extension: how the West was widened. *Annual Review of Earth and Planetary Sciences* **27**, 417-462 (1999).
68. Cowie PA*, et al.* Orogen-scale uplift in the central Italian Apennines drives episodic behaviour of earthquake faults. *Sci Rep* **7**, 44858 (2017).
69. Talone D, De Siena L, Lavecchia G, de Nardis R. The Attenuation and Scattering Signature of Fluid Reservoirs and Tectonic Interactions in the Central-Southern Apennines (Italy). *Geophysical Research Letters* **50**, (2023).

70. de Nardis R, Vuan A, Carbone L, Talone D, Romano MA, Lavecchia G. Interplay of tectonic and dynamic processes shaping multilayer extensional system in southern-central Apennines. *Sci Rep* **14**, 18375 (2024).
71. Bruno PP, Di Fiore V, Ventura G. Seismic study of the '41st Parallel' Fault System offshore the Campanian–Latial continental margin, Italy. *Tectonophysics* **324**, 37–55 (2000).
72. Weil AB, Sussman AJ. Classifying curved orogens based on timing relationships between structural development and vertical-axis rotations. In: *Orogenic curvature: Integrating paleomagnetic and structural analyses* (eds Sussman AJ, Weil AB). Geological Society of America (2004).
73. Buttinelli M, Improta L, Bagh S, Chiarabba C. Inversion of inherited thrusts by wastewater injection induced seismicity at the Val d'Agri oilfield (Italy). *Scientific Reports* **6**, 1-8 (2016).
74. Improta L, De Gori P, Chiarabba C. New insights into crustal structure, Cenozoic magmatism, CO2degassing, and seismogenesis in the southern Apennines and Irpinia region from local earthquake tomography. *Journal of Geophysical Research: Solid Earth* **119**, 8283-8311 (2014).
75. Feriozzi F, Improta L, Maesano FE, De Gori P, Basili R. The 3D Crustal Structure in the Epicentral Region of the 1980, Mw 6.9, Southern Apennines Earthquake (Southern Italy): New Constraints From the Integration of Seismic Exploration Data, Deep Wells, and Local Earthquake Tomography. *Tectonics* **43**, (2024).
76. Morley CK. Extension detachments and sedimentation in continental rifts (with particular reference to East Africa. *Tectonics* **8**, 1175-1192 (1989).
77. Vannoli P, Martinelli G, Valensise G. The Seismotectonic Significance of Geofluids in Italy. *Frontiers in Earth Science* **9**, (2021).
78. Pirrotta C*, et al.* Recent Activity and Kinematics of the Bounding Faults of the Catanzaro Trough (Central Calabria, Italy): New Morphotectonic, Geodetic and Seismological Data. *Geosciences* **11**, (2021).
79. Maesano FE, Tiberti MM, Basili R. The Calabrian Arc: three-dimensional modelling of the subduction interface. *Sci Rep* **7**, 8887 (2017).
80. Carafa MMC, Kastelic V, Bird P, Maesano FE, Valensise G. A "Geodetic Gap" in the Calabrian Arc: Evidence for a Locked Subduction Megathrust? *Geophysical Research Letters* **45**, 1794-1804 (2018).
81. Pastori M*, et al.* The 2011–2014 Pollino Seismic Swarm: Complex Fault Systems Imaged by 1D Refined Location and Shear Wave Splitting Analysis at the Apennines–Calabrian Arc Boundary. *Frontiers in Earth Science* **Volume 9 - 2021**, (2021).
82. Aki K. Characterization of barriers on an earthquake fault. *Journal of Geophysical Research: Solid Earth* **84**, 6140-6148 (1979).
83. Horváth F*, et al.* Evolution of the Pannonian basin and its geothermal resources. *Geothermics* **53**, 328-352 (2015).
84. Sibuet J-C, Yeh Y-C, Lee C-S. Geodynamics of the South China Sea. *Tectonophysics* **692**, 98-119 (2016).
85. Lavecchia G, Brozzetti F, Barchi M, Menichetti M, Keller JVA. Seismotectonic zoning in east-central Italy deduced from an analysis of the Neogene to present deformations and related stress fields. *Geological Society of America Bulletin* **106**, 1107-1120 (1994).
86. D'Agostino N, Giuliani R, Mattone M, Bonci L. Active crustal extension in the Central Apennines (Italy) inferred from GPS measurements in the interval 1994–1999. *Geophysical Research Letters* **28**, 2121-2124 (2001).

87. Devoti R*, et al.* A Combined Velocity Field of the Mediterranean Region. *Annals of Geophysics* **60**, (2017).
88. Artemieva IM, Mooney WD. On the relations between cratonic lithosphere thickness, plate motions, and basal drag. *Tectonophysics* **358**, 211-231 (2002).
89. Barba S, Carafa MMC, Boschi E. Experimental evidence for mantle drag in the Mediterranean. *Geophysical Research Letters* **35**, (2008).
90. Delvaux D, Sperner B. New aspects of tectonic stress inversion with reference to the TENSOR program. *Geological Society, London, Special Publications* **212**, 75-100 (2003).
91. Palano M. On the present-day crustal stress, strain-rate fields and mantle anisotropy pattern of Italy. *Geophysical Journal International* **200**, 969-985 (2015).
92. Carafa MMC, Bird P. Improving deformation models by discounting transient signals in geodetic data: 1. Concept and synthetic examples. *Journal of Geophysical Research: Solid Earth* **121**, 5538-5556 (2016).
93. Pietrolungo F*, et al.* Comparison of Crustal Stress and Strain Fields in the Himalaya–Tibet Region: Geodynamic Implications. *Remote Sensing* **16**, (2024).
94. Galadini F*, et al.* Time intervals to assess active and capable faults for engineering practices in Italy. *Engineering Geology* **139-140**, 50-65 (2012).
95. Machette MN. Active, capable, and potentially active faults: a paleoseismic perspective. *Journal of Geodynamics* **29**, 387-392 (2000).
96. Christophersen A*, et al.* Development of the Global Earthquake Model's neotectonic fault database. *Natural Hazards* **79**, 111-135 (2015).
97. Zelenin E, Bachmanov D, Garipova S, Trifonov V, Kozhurin A. The Active Faults of Eurasia Database (AFEAD): the ontology and design behind the continental-scale dataset. *Earth System Science Data* **14**, 4489-4503 (2022).
98. Zaccagnino D, Doglioni C. Fault dip vs shear stress gradient. *Geosystems and Geoenvironment* **2**, (2023).
99. Aki K, Richards P. *Quantitative Seismology*, 2nd edn. University Science Books U.S. (2002).
100. Spada M, Bianchi I, Kissling E, Agostinetti NP, Wiemer S. Combining controlled-source seismology and receiver function information to derive 3-D Moho topography for Italy. *Geophysical Journal International* **194**, 1050-1068 (2013).
101. Sparacino F, Galuzzi BG, Palano M, Segou M, Chiarabba C. Seismic coupling for the Aegean - Anatolian region. *Earth-Science Reviews* **228**, (2022).
102. Tape C, Musé P, Simons M, Dong D, Webb F. Multiscale estimation of GPS velocity fields. *Geophysical Journal International* **179**, 945-971 (2009).